Population receptive fields in non-human primates from whole-brain fMRI and large-scale neurophysiology in visual cortex

P. Christiaan Klink[1,2*], Xing Chen[1], Wim Vanduffel[3,4,5,6] & Pieter R. Roelfsema[1,2,7]

[1] Netherlands Institute for Neuroscience, Royal Netherlands Academy of Arts and Sciences, Amsterdam, Meibergdreef 47, 1105 BA Amsterdam, The Netherlands.
[2] Psychiatry Department, Amsterdam UMC, Meibergdreef 9, 1105 AZ Amsterdam, The Netherlands.
[3] Laboratory for Neuro- and Psychophysiology, Department of Neurosciences, KU Leuven Medical School, 3000, Leuven, Belgium.
[4] Massachusetts General Hospital, Martinos Ctr. for Biomedical Imaging, Charlestown, MA, 02129, USA.
[5] Leuven Brain Institute, KU Leuven, 3000, Leuven, Belgium.
[6] Harvard Medical School, Boston, MA, 02115, USA.
[7] Department of Integrative Neurophysiology, Center for Neurogenomics and Cognitive Research, VU University, De Boelelaan 1085, 1081 HV Amsterdam, The Netherlands.

***Corresponding author:**
P.C. Klink
Netherlands Institute for Neuroscience
Meibergdreef 47, 1105BA, Amsterdam, The Netherlands
Email: c.klink@nin.knaw.nl
Phone: +31(0)20 5664581
Fax: +31(0)20 5666121

Ethics statement

Animal care and experimental procedures were in accordance with the ILAR's Guide for the Care and Use of Laboratory Animals, the European legislation (Directive 2010/63/EU) and approved by the institutional animal care and use committee of the Royal Netherlands Academy of Arts and Sciences and the Central Authority for Scientific Procedures on Animals (CCD) in the Netherlands.

Conflicts of interest

The authors declare that no financial or non-financial competing interests exist.

Data and code availability

All data and code are available on GIN: https://doi.org/10.12751/g-node.p8ypgv
Unthresholded fMRI model fitting results are on Neurovault: https://identifiers.org/neurovault.collection:8082

Abstract

Population receptive field (pRF) modeling is a popular fMRI method to map the retinotopic organization of the human brain. While fMRI-based pRF-maps are qualitatively similar to invasively recorded single-cell receptive fields in animals, it remains unclear what neuronal signal they represent. We addressed this question in awake non-human primates comparing whole-brain fMRI and large-scale neurophysiological recordings in areas V1 and V4 of the visual cortex. We examined the fits of several pRF-models based on the fMRI BOLD-signal, multi-unit spiking activity (MUA) and local field potential (LFP) power in different frequency bands. We found that pRFs derived from BOLD-fMRI were most similar to MUA-pRFs in V1 and V4, while pRFs based on LFP gamma power also gave a good approximation. FMRI-based pRFs thus reliably reflect neuronal receptive field properties in the primate brain. In addition to our results in V1 and V4, the whole-brain fMRI measurements revealed retinotopic tuning in many other cortical and subcortical areas with a consistent increase in pRF-size with increasing eccentricity, as well as a retinotopically specific deactivation of default-mode network nodes similar to previous observations in humans.

Introduction

The concept of a receptive field (RF) is crucial for our understanding of the mechanisms underlying perception, cognition, and action. Receptive fields (RFs) (Hartline, 1938; Sherrington, 1906) typically describe stimulus locations that evoke or modulate neuronal responses, but they can be generalized to different stimulus features such as color or spatial frequency. RFs are usually measured by determining the neuronal firing rate elicited by visual stimuli, (Hubel and Wiesel, 1998, 1968, 1959), but they can also be defined based on other neuronal signals such as subthreshold activity (Priebe, 2008), properties of the local field potential (Victor et al., 1994), or calcium levels that can, for instance, be measured with fluorescent calcium indicators (Beest et al., 2021; Bonin et al., 2011).

Non-invasive methods lack the spatial resolution to measure the RF properties of single neurons, but they can characterize the RF properties of the aggregate neural signals being measured. The retinotopic organization of the human brain has now been characterized with functional magnetic resonance imaging for decades (Wandell et al., 2007; Wandell and Winawer, 2010). Early studies used phase-encoding with 'rotating wedge' and 'expanding or contracting ring' stimuli to identify RF position (Engel, 2012; Engel et al., 1994; Sereno et al., 1995), while later studies increasingly used the 'population receptive field' (pRF) method that estimates RF-size in addition to position (Dumoulin and Wandell, 2008; Wandell et al., 2007; Wandell and Winawer, 2015, 2010). The method is popular and has been used to map a range of visual and cognitive functions (Binda et al., 2018; Ekman et al., 2020; Harvey et al., 2020, 2015; He et al., 2019; Hughes et al., 2019; Mo et al., 2017; Poltoratski et al., 2019; Poltoratski and Tong, 2020; Puckett et al., 2020; Shao et al., 2013; Shen et al., 2020; Silson et al., 2018; Stoll et al., 2020; Thomas et al., 2015; Welbourne et al., 2018; Zuiderbaan et al., 2017), dysfunctions (Ahmadi et al., 2020; Alvarez et al., 2020; Best et al., 2019; Dumoulin and Knapen, 2018;

Green et al., 2019; Schwarzkopf et al., 2014), mechanisms of brain development (Dekker et al., 2019), cortical evolution (Keliris et al., 2019; Kolster et al., 2014; Zhu and Vanduffel, 2019), and information transfer across different brain areas (Haak et al., 2013).

The term 'pRF' highlights the analogy to neuronal RFs. It assumes that the blood-oxygen-level-dependent signal (BOLD) measured with fMRI reflects the aggregate response of a large population of neurons within a voxel. Indeed, pRFs of the human visual cortex are qualitatively similar to the RFs of single neurons or multi-unit activity in animals (Dumoulin and Wandell, 2008). However, most of the previous comparisons were between species, and between studies that used different techniques to measure pRFs/RFs (Barlow et al., 1966; Hubel and Wiesel, 1968). Exceptions are pRF studies based on intracranial recordings in human patients (Harvey et al., 2013; Winawer et al., 2013), which used a limited number of surface electrodes to measure ECoG or intracranial EEG, but not spiking activity. The pRFs derived from the local field potential (LFP) exhibited similar properties to pRFs derived from BOLD signals, including similar spatial summation characteristics (Winawer et al., 2013). Another study compared BOLD-based pRFs in monkeys to the RF properties of single units in published work (Kolster et al., 2014). Furthermore, Keliris et al. (2019) found that single unit RFs in one of their monkeys were smaller than pRFs measured with BOLD and proposed another method to estimate RF sizes. Their study included MUA but not the LFP. A systematic within-species comparison of pRFs derived from BOLD, MUA and LFP has however never been carried out.

Here, we fill that gap with extensive pRF modeling based on BOLD, MUA and LFP signals in macaque monkeys. The question which neuronal signal forms the basis of the fMRI BOLD signal has far-reaching consequences for the interpretation of human neuroimaging results and is therefore a topic of ongoing debate and rigorous investigation (Arthurs and Boniface, 2002; Bartels et al., 2008; Boynton, 2011; Drew, 2019; Ekstrom, 2010; Goense and Logothetis, 2008; Logothetis, 2010, 2003; Logothetis et al., 2001; Logothetis and Wandell, 2004; Maier et al., 2008; Scholvinck et al., 2010; Sirotin and Das, 2009; Winawer et al., 2013; Winder et al., 2017). Some studies reported that properties of the BOLD signal resemble features of both neuronal spiking and the local field potential (LFP) (Mukamel et al., 2005; Nir et al., 2007; Rees et al., 2000), others that they resemble the LFP but not spiking (Bartolo et al., 2011; Maier et al., 2008; Niessing et al., 2005; Viswanathan and Freeman, 2007), and yet others that they resemble spiking rather than the LFP (Lima et al., 2014). Here we examine the degree to which pRFs based on the BOLD signal resemble pRFs based on spiking activity and distinct frequency bands of the LFP (Buzsaki, 2006, 2004; Einevoll et al., 2013; van Kerkoerle et al., 2014). In non-human primates, we measured BOLD-pRFs using whole-brain fMRI and determined neuronal pRFs with large-scale neurophysiological recordings in V1 and V4 (Figure 1). Besides showing the presence of retinotopic information throughout the brain based on the fMRI data, we could directly compare V1 and V4 pRFs obtained with fMRI and electrophysiology. This intraspecies comparison provides new insight into the neurophysiological basis of the BOLD-defined pRFs and offers a benchmark for visual field maps obtained with fMRI.

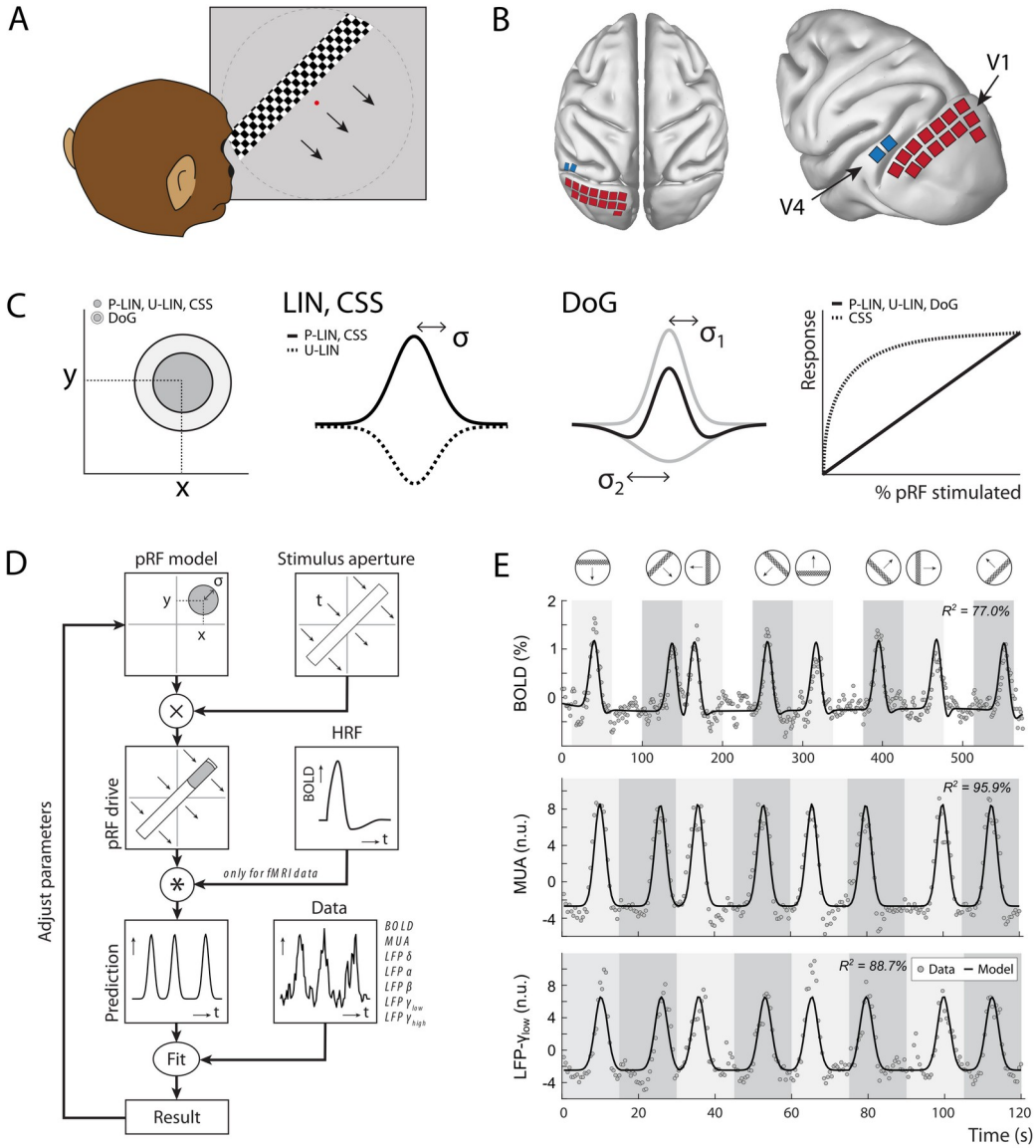

Figure 1. Experimental set-up and study design. (A) Monkeys maintained fixation on a red dot while bars with high-contrast moving checkerboards moved across the screen in eight different directions behind a virtual aperture (dashed line, not visible in the real stimulus). **(B)** Two animals performed the task in the MRI-scanner. Two other animals were each implanted with 16 Utah arrays (1,024 electrodes/animal) in the left visual cortex. The approximate locations of 14 V1 arrays (red) and 2 V4 arrays (blue) for one animal are depicted on the NMT standard macaque brain. For more detailed array configurations see Chen et al. (2020). **(C)** Four pRF models were fit to the data, differing in their pRF parameters (location: x,y; size: σ) and spatial summation characteristics. The Difference-of-Gaussians (DoG) pRFs are described by an excitatory center and an inhibitory surround (both 2D Gaussians with σ_1 and σ_2 as size parameters; dark and light gray circles in the left panel, respectively). Other models fitted single Gaussians that were either constrained to be positive (second panel: solid line) or allowed to be negative (unconstrained linear U-LIN, dashed line). The CSS model implemented non-linear spatial summation across the RF (fourth panel: dashed line), while all other models implemented linear summation (solid line). **(D)** The pRF model fitting procedure. A model pRF is multiplied with an 'aperture version' of the bar stimulus to generate a predicted response. For fMRI data this prediction was convolved with a monkey specific HRF. The difference between the recorded neural signal (BOLD, MUA, LFP) and the predicted response was minimized by adjusting the pRF model parameters. **(E)** Examples of data and model fits for a V1 voxel (top panel), and a V1-electrode (middle and bottom panel). Average activity (gray data points) depicts the BOLD signal (top), MUA (middle) and LFP-power in the low gamma band (bottom). Black lines are the model fits for a P-LIN pRF model. Light and dark gray areas depict visual stimulation periods (bar sweeps as indicated by the icons above). In the white epochs, the animals viewed a uniform gray background to allow the BOLD signal to return to baseline (these epochs were not necessary in the electrophysiology recordings). Note that that in MRI trials, the bar stimuli had a lower speed (1 TR or 2.5 s per stimulus location) than during electrophysiology (500 ms per stimulus location).

The original method of estimating pRFs from BOLD responses (Dumoulin and Wandell, 2008) uses a forward modeling approach to fit the location and size of a symmetrical two-dimensional Gaussian to the BOLD responses. This approach is often used to predict neuronal activity elicited by moving bar-shaped stimuli. The RF model minimizes the difference between measured and predicted responses by multiplying the pRF with the stimulus and convolving the result with a hemodynamic response function (HRF), which accounts for the time-course of neurovascular coupling (Figure 1). Later refinements implemented a Difference-of-Gaussians pRF profile (DoG) to account for center-surround interactions (Zuiderbaan et al., 2012) (Figure 1C), with substantial improvements in early visual cortex. Another refinement is the introduction of a static non-linearity that models non-linear spatial summation across RFs (Britten and Heuer, 1999; Kay et al., 2013; Oleksiak et al., 2011; Winawer et al., 2013). In such a model, the best parameters indicate sub-additive spatial summation in all visual areas (Kay et al., 2013). This means that if stimulus S_1 elicits a response R_1 and a non-overlapping stimulus S_2 elicits response R_2, the response to the combined stimulus, S_1+S_2, is smaller than the sum, R_1+R_2. For this reason, the non-linear spatial summation model has also been called the 'compressive spatial summation' (CSS) model. A third extension has been the modeling of negative pRFs. Standard approaches tend to only include voxels that show increases in the BOLD signal in response to a stimulus. The inclusion of 'negative' pRFs with decreased BOLD activity has revealed the retinotopic organization of a number of areas in the so-called default mode network (DMN) (Szinte and Knapen, 2019). In our analysis of pRFs based on BOLD, MUA and LFPs, we explored several pRF models, allowing us to investigate the potential presence of nonlinear spatial summation and negative pRFs.

Results

Four macaque monkeys (*Macaca mulatta*) participated in this study. They were rewarded with fluid for maintaining their gaze inside a 1.5° window around a fixation point that was presented at the center of a frontoparallel screen. While they fixated, a 2° wide bar containing full-contrast moving checkerboards traversed the screen in eight different directions (Figure 1). Two animals performed this task in a 3T horizontal bore MRI scanner. Two other monkeys were each implanted with 1,024 electrodes in the visual cortex (V1, V4). They performed the same task while neuronal activity (MUA and LFP) was recorded simultaneously from all electrodes. In the MRI setup, the stimulus covered 16° of the visual field, which was the maximum possible with the monitor located just outside of the scanner bore. The bar traveled across this screen in 20 steps of 2.5 s (1 TR). In the electrophysiology setup, the monitor was closer to the animal, allowing a visual field coverage of 28°. The stimulus bar moved across this aperture in 30 steps of 500 ms. For both the MRI and electrophysiology recordings, we only included data from epochs when the animals maintained fixation for >80% of the time.

After preprocessing (see Materials and Methods) we independently fit four pRF models to the average BOLD time-courses. These models were: (1) a linear pRF model constrained to have positive responses (P-LIN) (Dumoulin and Wandell, 2008), (2) an unconstrained version of the linear pRF model that can also model

negative responses (U-LIN), (3) a difference-of-Gaussians pRF model (DoG) (Zuiderbaan et al., 2012), and (4) a non-linear 'compressive spatial summation' (CSS) pRF model (Kay et al., 2013) (Figure 1). We used the fitting method to determine pRF size, shape and location. A cross-validated goodness of fit (R^2) was determined by fitting the model to one half of the data and calculating R^2 using the other half of the data. Cross-validation allows the comparison of fit quality between models with different numbers of parameters.

PRFs measured with BOLD fMRI

All models provided good fits to the BOLD time-courses in a range of cortical and subcortical areas known to be involved in visual processing. For both monkeys (M1 & M2), we found robust retinotopic information in occipital, temporal, and parietal cortex (Figure 2). PRFs in all these areas were in the contralateral visual field and retinotopic maps were consistent with previous reports (Figure 2B), some of which were more extensive (Arcaro et al., 2011; Arcaro and Livingstone, 2017; Brewer et al., 2002; Janssens et al., 2014; Kolster et al., 2014; Rima et al., 2020; Zhu and Vanduffel, 2019). Weaker and sparser retinotopic information was also observed in the frontal cortex, e.g. around the arcuate sulcus (area 8, including the Frontal Eye Fields) and in the ventrolateral prefrontal cortex (VLPFC). Throughout this study, we will use a voxel inclusion criterion of $R^2 > 5\%$ unless otherwise noted. While R^2 was generally much higher in visual areas (Figure 2A, bottom panel) this relatively low threshold also reveals retinotopic information in more frontal areas and some subcortical regions (where the signal picked up by surface coils has a lower signal-to-noise ratio). Figure 2C shows the number of voxels within a range of areas for which the models explained more than 5% of the variance (Supplemental Figure 1 shows the proportion per ROI). The functional parcellation of visual areas based on field sign inversions around horizontal and vertical meridians lined up well with a probabilistic atlas, co-registered to the individual animal's anatomy (D99, Reveley et al., 2016).

Subcortically, we could segregate the lateral geniculate nucleus (LGN), pulvinar and some striatal regions from their surrounding areas on the basis of a higher R^2. In both monkeys, the LGN of both hemispheres contained clear retinotopic maps (Figure 3A). Retinotopic information was also evident in the bilateral pulvinar of M1, but some of the pRFs in the pulvinar of M2 were large and crossed the vertical meridian, resulting in noisy polar angle maps (Figure 3B). Striatal retinotopy was less pronounced in M1 and even more variable in terms of polar angle maps (Supplemental Figure 2).

We calculated cross-validated R^2 values to compare the four pRF models: P-LIN, U-LIN, DoG and CSS (Figure 1C). A comparison of model performance pooled over subjects and voxels confirmed that there were significant differences across models, with the CSS model outperforming the P-LIN model (Kruskal-Wallis test on all four models, $H = 21.33$, $df = 3$, $p < 0.0001$; post-hoc Tukey's HSD multiple comparisons of mean rank, $R^2_{CSS} > R^2_{P\text{-}LIN}$, $p < 0.0001$). Indeed, the CSS model fit was better than that of P-LIN in all ROIs in M1 and in 38 out of 39 ROIs in M2 (Wilcoxon signed rank, $p < 0.05$; no difference in premotor area F7 in M2) (Figure 4). Since the CSS model also provided the best fits for the neurophysiological signals (described later), we report results from this model and only extend the analysis to other models where this is useful (e.g.

in the case of negative gain values). The advantage of the CSS model over the P-LIN model generally increased in higher visual areas (Supplemental Figure 3).

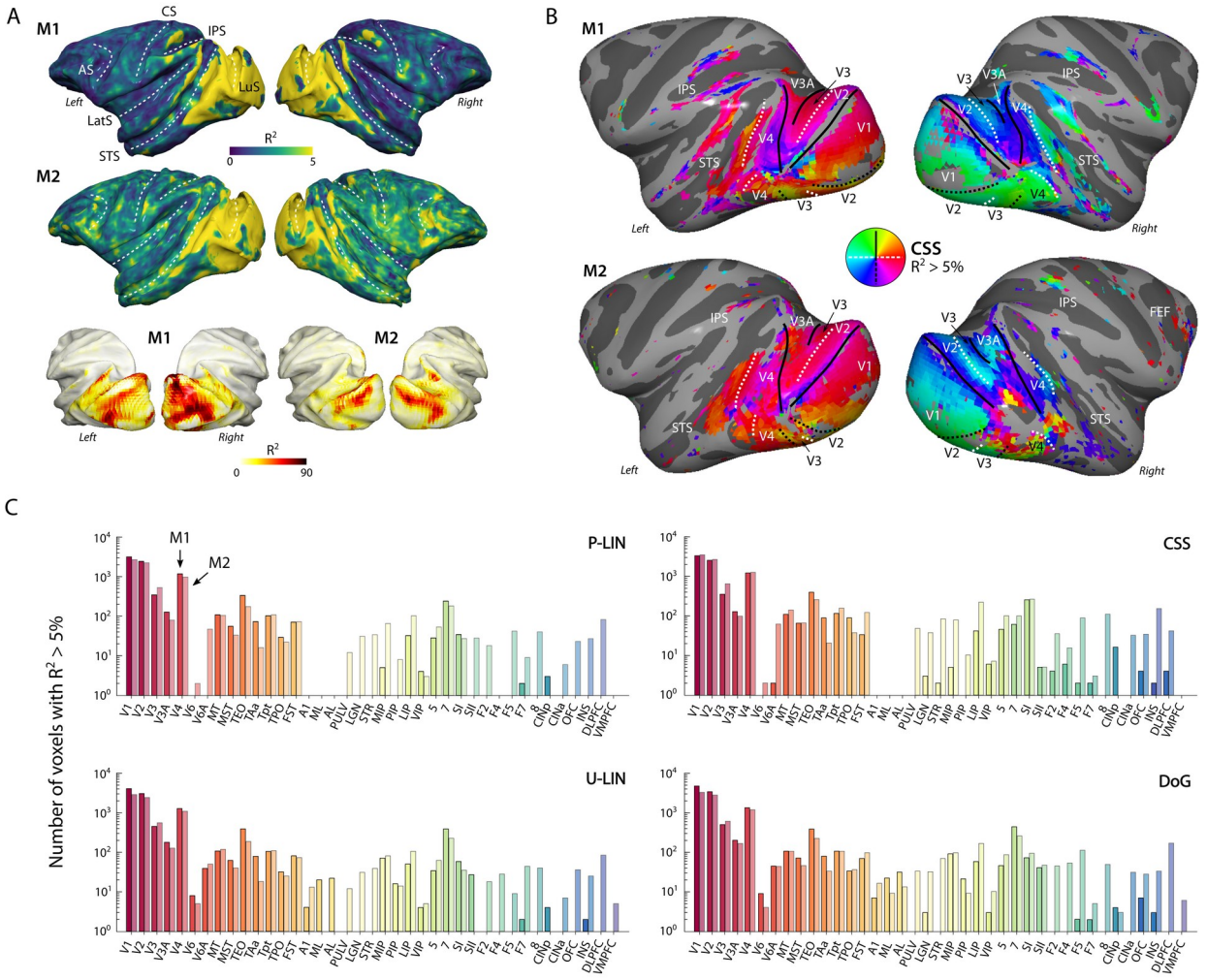

Figure 2. PRF model fits and retinotopic maps. (A) R^2 value map of the CSS pRF-model projected on the surface rendering of the brains of two monkeys (M1, M2). The lower panel illustrates that the R^2 value in the visual cortex is generally much higher than 5% (going up to ~90%). The color range in the upper panels also reveals the weaker retinotopic information elsewhere in the cortex. (AS: Arcuate Sulcus; CS: Central Sulcus; IPS: Intraparietal Sulcus; LatS: Lateral Sulcus; LuS: Lunate Sulcus; STS: Superior Temporal Sulcus) **(B)** Polar angle maps for both subjects from the CSS model, thresholded at $R^2 > 5\%$, displayed on the inflated cortical surfaces. Functional delineation of several visual areas is superimposed. (FEF: Frontal Eye Fields). **(C)** Number of (resampled) voxels with $R^2 > 5\%$ per brain area and subject for each model. Note the logarithmic scale. See Supplemental Figure S1 for proportions per ROI, and Supplemental Table 1 for all ROI abbreviations.

The static nonlinearity parameter, or 'pRF exponent' that models the nonlinearity of spatial summation (Materials and Methods: Equation 4) was in the range of 0.2-0.4 and significantly below one in all areas (Wilcoxon Signed Rank, one-tailed, all ROIs with more than four voxels $R^2 > 5\%$, $p < 0.001$). These values of the pRF exponent represent sub-additive (compressive) spatial summation, in accordance with observations in

the human visual cortex (Kay et al., 2013; Winawer et al., 2013). The pRF exponent in early visual cortex is comparable to previously reported values for human V1. The exponent value in higher visual areas was similar to that in early visual cortex of the two monkeys, and higher than previously observed in human extrastriate cortex, which suggests that spatial suppression is less pronounced in higher areas of the monkey visual cortex than in higher areas of the human visual cortex.

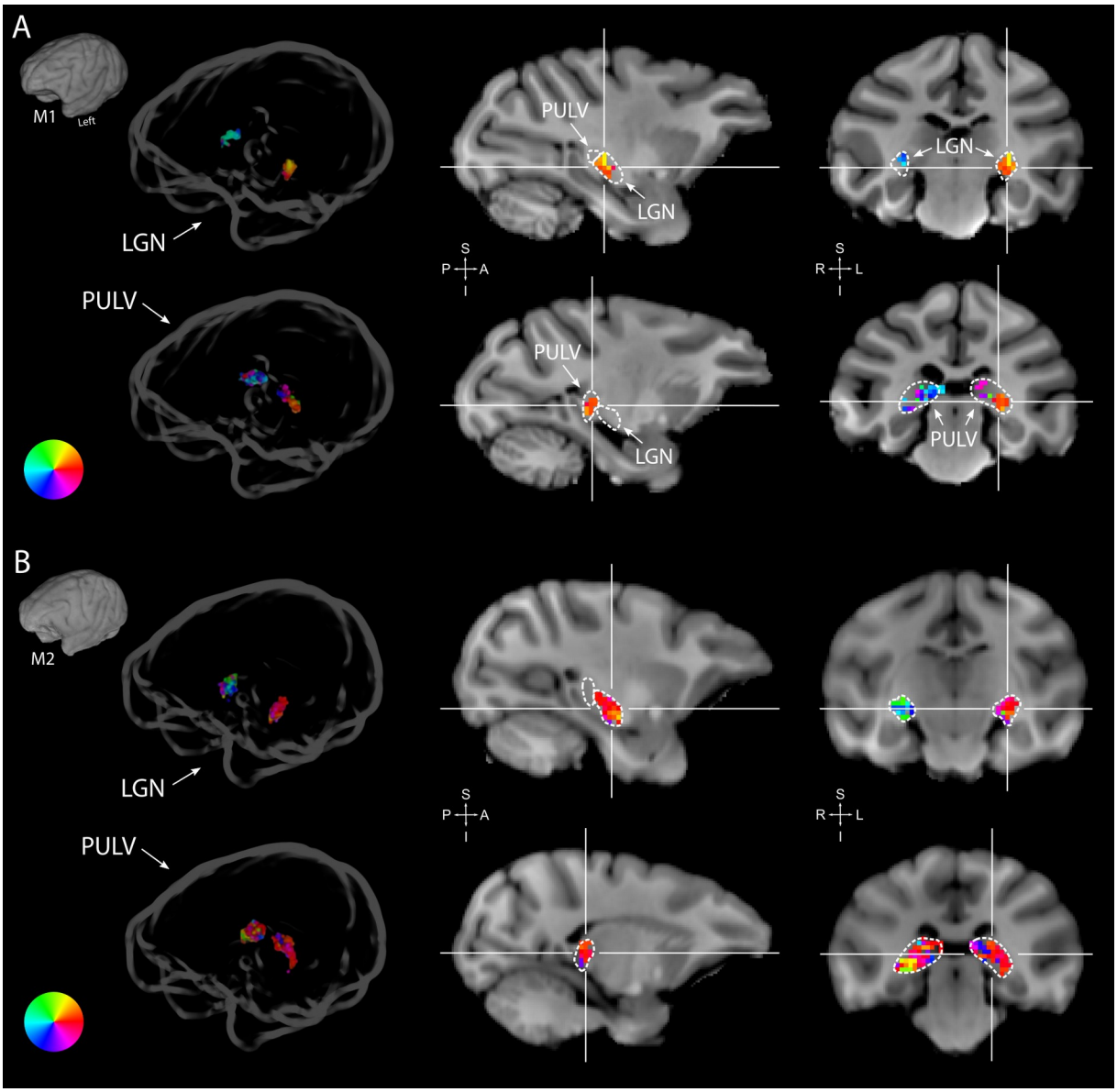

Figure 3. Retinotopy in the thalamus. Thalamic pRFs in M1 **(A)** and M2 **(B)**. The lateral geniculate nucleus (LGN, top rows) contained retinotopic maps of the contralateral visual field in both monkeys (M1: 38/38; M2: 73/80 voxels with contralateral pRFs). Retinotopic information was also present in the pulvinar (PULV, bottom rows), but its organization was much less structured, especially in M2 (M1: 23/32; M2: 61/131 voxels with contralateral pRFs). Voxels were thresholded at $R^2 > 3\%$ for these polar angle visualizations, due to the generally poorer fits in subcortex compared to visual cortex. Results from the CSS model are masked by ROI and shown both in a 'glass' representation of the individual animals' brains (left), and on selected sagittal and coronal slices (monkey-specific T1-weighted images, cross-hairs indicate slice positions). Dashed lines indicate the boundaries of the LGN and pulvinar.

Both the U-LIN model and the DoG model also performed better than the standard P-LIN model (Kruskal-Wallis, Tukey's HSD, both ps < 0.0001). The DoG had slightly better fits across all pooled voxels than the U-LIN model (Kruskal-Wallis, Tukey's HSD, p < 0.0001). The advantage of the DoG model over the P-LIN model was most pronounced in V1 and decreased in higher visual areas.

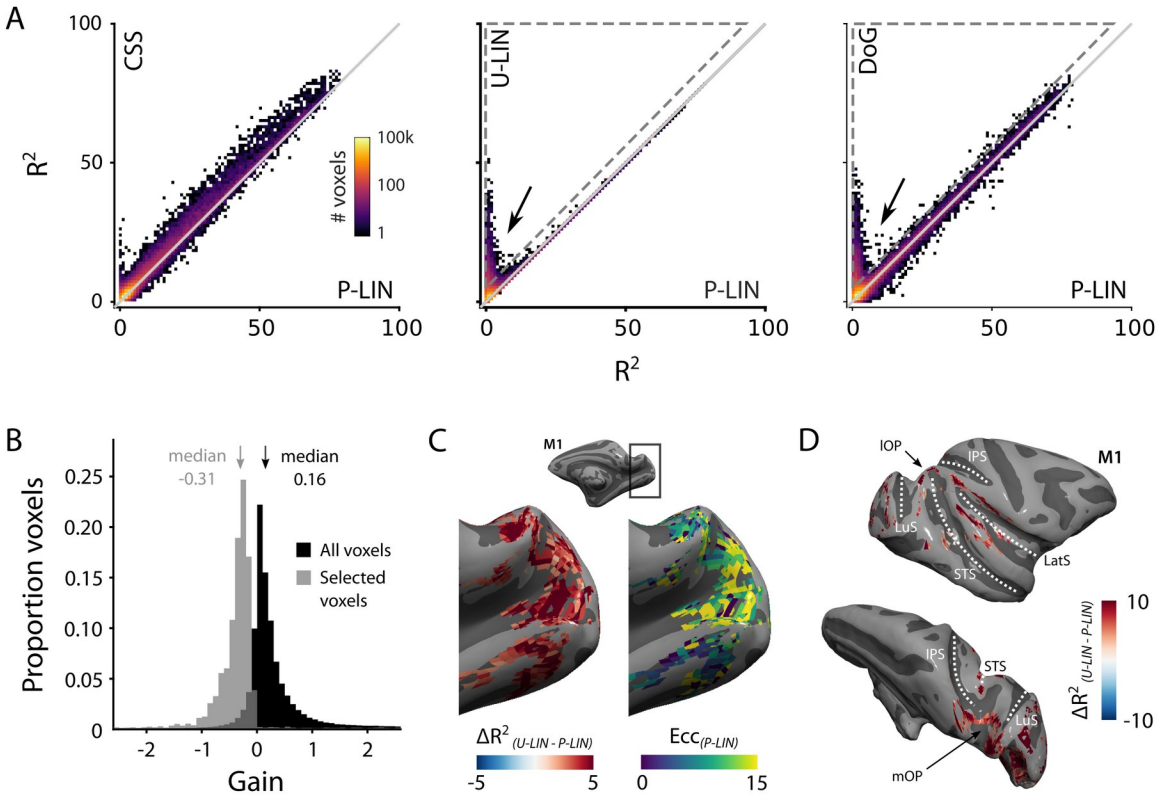

Figure 4. Comparison of the four pRF models. (A) Comparison across pRF models. R^2 data is in bins of 1% × 1%, and color indicates the number of voxels per bin. The CSS model fits the data best, while U-LIN and DoG models give better fits for voxels that are poorly characterized by the P-LIN model (arrows). Dashed triangle, voxels for which R^2 of the U-LIN/DoG models was at least 5% higher than that of the P-LIN model. **(B)** Gain values of the U-LIN pRF fits for all voxels (black) and the voxels in the gray triangle in **A**. The negative gain values indicate visual suppression of the BOLD signal. Arrows, medians. **(C)** Clusters of voxels for which the U-LIN model fit better than the P-LIN model were located in the medial occipital lobe (left panel). The pRFs of these voxels had a high eccentricity according to the P-LIN model, beyond the stimulated visual field. **(D)** Clusters of voxels with negative pRFs in the U-LIN model (without positive pRFs in the P-LIN model) were present around the lateral sulcus (LatS), in the medial occipital parietal cortex (mOP) and in the lateral occipital parietal cortex (lOP).

Negative pRFs from suppressed BOLD responses

There was a subset of voxels with negative BOLD responses for which both the U-LIN and DoG models provided much better pRF fits than the P-LIN and CSS models (arrows in Figure 4A, Supplemental Figure 3C). We inspected the voxels for which the R^2 in the U-LIN/DOG models was at least 5% higher than in the P-LIN model (gray, dashed triangles in Figure 4A). The U-LIN model estimated a negative gain for these voxels (median gain = -0.31, Wilcoxon Signed Rank, one-tailed, z = -43.9, p < 0.0001) (Figure 4B) and the

DoG model returned a high level of inhibition (median normalized suppressive amplitude = 1.14, Interquartile range (IQR), 0.98-1.29).

There were two categories of voxels with negative responses (Supplemental Figure 4). For the first category of voxels, the P-LIN model estimated pRFs outside the boundaries of the stimulated visual field. This result suggests that the negative response represents surround suppression that is particularly strong around the fovea (Sereno et al., 1995; Shmuel et al., 2006; Smith et al., 2004). The retinotopy of these voxels is consistent with this explanation. In V1, for instance, the voxels were on the medial side of the occipital pole, which represents the peripheral visual field (Figure 4C). The second category of voxels with negative pRFs appeared to be different. Here P-LIN and CSS models could not fit any pRF, suggesting purely negative BOLD responses. These voxels were primarily located in the medial occipital parietal cortex (mOP), at the superior border of the superior temporal sulcus in the lateral occipital parietal cortex (lOP) and around the lateral sulcus (LatS) which includes parts of the insula, cingulate, parietal, and premotor cortices (Figure 4D). These areas have all previously been identified as being part of the monkey default mode network (DMN) (Mantini et al., 2011). This finding aligns with recent research in humans that revealed similar negatively tuned pRFs in corresponding nodes of the human DMN (Szinte and Knapen, 2019)

PRF size as a function of eccentricity

As expected, pRF sizes were larger at higher eccentricities. This relationship was evident in all areas with larger numbers of well-fit voxels. PRFs were also larger in higher areas, which exhibited a steeper slope of the eccentricity-size relationship (Figure 5; Supplemental Figure 5A,B). The differences between the slopes in V1 and V2 are smaller than expected based on previous electrophysiological studies, but this is not uncommon with fMRI (Kay et al., 2013). In one animal, we also unexpectedly observed retinotopy in a number of higher areas, such as the anterior cingulate cortex (Supplemental Figure 5). This brain region has been studied predominantly in the context of decision-making (Amiez et al., 2006; Fouragnan et al., 2019) but it does have resting state correlations with V1 (Griffis et al., 2017). Our design lacked the power for a more detailed investigation of this retinotopic organization, but this result may inspire future work on brain-wide retinotopic tuning.

Multi-unit spiking activity RFs

We determined the RFs of multi-unit activity recorded with chronically implanted electrode arrays (Utah arrays) in areas V1 and V4 in two additional monkeys (M3 and M4) that did not participate in the fMRI experiments. We used a 1,024-channel cortical implant, consisting of a titanium pedestal that was connected to 16 Utah arrays (Rousche and Normann, 1998). Each Utah array had 8x8 shanks with a length of 1.5 mm. In both monkeys, 14 arrays were placed in V1 and two in V4 of the left hemisphere (Figure 6). The stimulus was similar to that used in the fMRI experiments with some small differences due to constraints of the two setups (in the electrophysiology setup the stimulus covered a larger portion of the visual field because the screen was closer to the animal) and the intrinsic nature of the recorded signals (stimulus steps were faster in the

electrophysiology experiments because the electrophysiology signals are much faster than the BOLD response). We fit the four pRF models to the MUA responses and to the LFP power in five distinct frequency bands. We compared the MUA pRFs to a more conventional MUA RF-mapping method (cRFs). For this cRF method, we selected channels with a signal-to-noise ratio (SNR) larger than three (i.e., visual responses that were more than three times larger than the standard deviation of the spontaneous activity) and derived the RF borders from the onset and offset of the neuronal activity elicited by a smoothly moving light bar (see Materials and Methods). Whenever both methods were able to estimate a pRF and cRF (R^2 > 25% for the pRF method, SNR > 3 and R^2 > 25% for the cRF method), the estimated locations were highly similar (median distance between pRF and cRF center, V1: 0.34, IQR 0.18 – 0.49 dva; V4: 0.90, IQR 0.40 – 1.41 dva). Compared to the P-LIN pRF-model, the moving-bar method estimated smaller cRFs (median size difference pRF_{sz}-cRF_{sz}: 0.50, IQR: 0.08-0.92)(Figure 7). The CSS model, however, returned pRF size estimates that were very similar to the cRF sizes or even a little bit smaller (median size difference pRF_{sz}-cRF_{sz}: -0.13, IQR: -0.41 – 0.14), suggesting that non-linear spatial summation might indeed be better at capturing the RF properties of a small population of neurons than linear summation.

The pRF models that used in this study are all based on circular (symmetric) receptive fields. A recent study (Silson et al., 2018) suggested that pRFs in human early visual cortex might be elliptical rather than circular, although this suggestion goes against previous work, although this suggestion goes against previous work (Greene et al., 2014; Merkel et al., 2018; Zeidman et al., 2018). A later study demonstrated that the elliptical fits were an artifact of the software that had been used in the analysis (Lerma-Usabiaga et al., 2021). The cRF method separately estimates the width and height of the receptive field, and can thus be used to calculate a simplified RF aspect ratio to investigate RF symmetry. While this measure differs from RF ellipticity (a 45° tilted ellipse has the same aspect ratio as a circle), it does provide some insight in the symmetry of the MUA RFs. We did observe a few cRFs with aspect ratios ($\sigma_{large}/\sigma_{small}$) that were larger than two (M3: 18/753; M4: 10/527; together 2.2% of all cRFS), but the vast majority of cRFs in both animals had aspect ratios close to one (M3 median: 1.12, IQR: 1.04 – 1.20; M4 median 1.13, IQR: 1.03 – 1.22) indicating near-symmetric RFs.

We obtained excellent fits to the MUA for all pRF models (see Figure 1E for an example fit). These pRFs covered a large proportion of the lower right visual field (Figure 6, Supplemental Figure 6). As expected, the pRFs from electrodes of the same arrays (shown in the same color in Figure 6) were clustered in space, and their locations were in accordance with established retinotopy (e.g., Hubel and Wiesel, 1974). The average R^2 (over all electrodes with R^2>0) was 64% in V1 (M3: 54%, M4: 73%) and 53% in V4 (M3: 37%, M4: 68%), which is substantially higher than the average R^2 of 11% in both V1 and V4 for the MRI data (all voxels with R^2>0; V1 M1: 14%, M2: 8%; V4 M1: 14%, M2: 8%).

Cross-validated comparisons revealed significant differences between the four models (Kruskal-Wallis test on all four models: H_{V1} = 204, df_{V1} = 3, p_{V1} < 0.0001; H_{V4} = 13.4, df_{V4} = 3, p_{V4} < 0.01) (Figure 8; similar patterns were present in each individual animal). Post-hoc pairwise comparisons (Tukey's HSD) revealed that the CSS and DoG models provided a better fit than the linear models, although for V4 the advantage of the CSS model

over the P-LIN model was only significant when electrodes with a poor fit ($R^2 < 25\%$) were excluded (V1, all electrodes: CSS vs. P-LIN, $p < 0.001$, DoG vs. P-LIN, $p < 0.001$; V4, all electrodes: CSS vs. P-LIN, $p = 0.16$, DoG vs. P-LIN, $p < 0.001$; V1, electrodes with $R^2 > 25\%$: CSS vs. P-LIN, $p < 0.001$, DoG vs. P-LIN, $p < 0.001$; V4, electrodes with $R^2 > 25\%$: CSS vs. P-LIN, $p < 0.02$, DoG vs. P-LIN, $p < 0.01$) (Figure 8). The improved fit of the DoG model was caused by the suppressive surround (median normalized suppressive amplitude = 0.71, IQR 0.56 – 0.86).

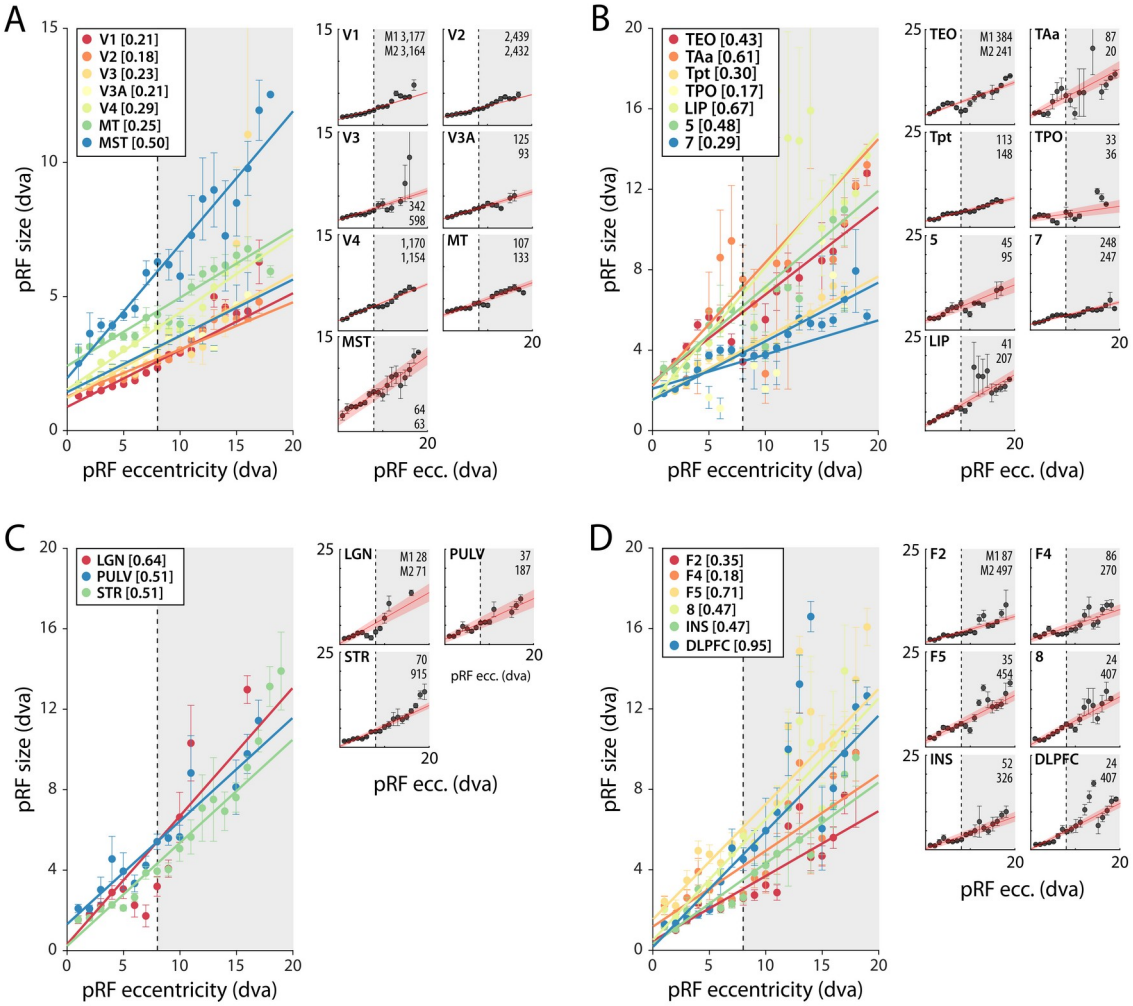

Figure 5. pRF size as function of eccentricity according to the CSS model. (A) Eccentricity-size relationship for early and mid-level visual areas. **(B)** Eccentricity-size relationship for areas in the temporal and parietal lobes. **(C)** Eccentricity-size relationship for subcortical areas. **(D)** Eccentricity-size relationship for frontal cortical areas. Data-points are pRF sizes binned in 2-dva-eccentricity bins; error bars denote SEM. Lines are linear fits with a significant slope ($p < 0.01$). Slope values are shown between square brackets in the legend. The dashed line that separates the white and gray areas indicates the extent of the visual stimulus used to estimate pRFs. Data points in the gray regions come for pRFs that fell partially outside the region with a visual stimulus. The small panels show the same data for individual areas and include confidence intervals of the linear fit (shaded red area). Numbers denote the number of voxels per animal. The displayed areas were selected based on the presence of at least 20 voxels in each animal, with $R^2 > 5\%$ for **(A,B)** and $R^2 > 3\%$ for **(C,D)** due to the generally lower fit quality in the subcortex and frontal lobe. Supplemental Figures 5 and 6 plot all suprathreshold voxels.

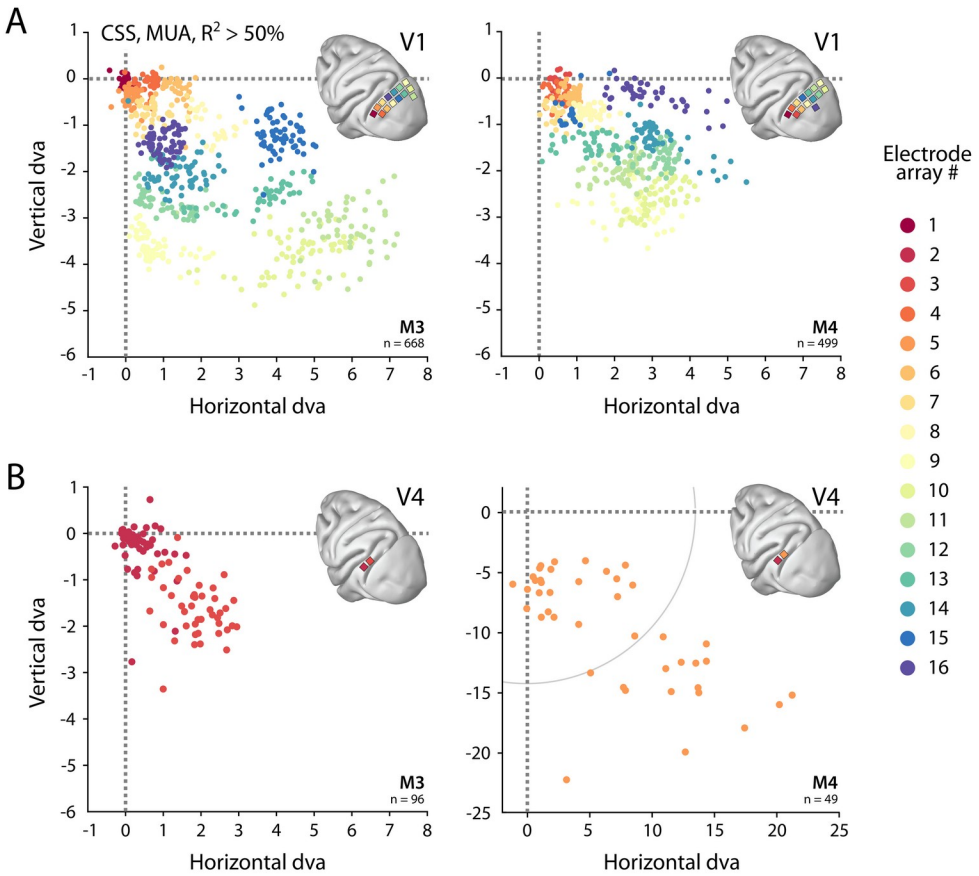

Figure 6. Visual field coverage of pRFs with Utah arrays. (A) In both monkeys (M3, M4), 14 Utah arrays were implanted on the left operculum that is partly V1. Different colors represent the center of MUA-based pRFs for the individual arrays. Only electrodes with R^2 > 50% in the CSS model are shown. **(B)** Same as in (A), but for V4 electrodes. Note the different scale in the lower right panel, with the gray arc indicating the extent of the visual stimulus. See Supplemental Figure 6 for pRF sizes.

The pRF exponent of the CSS model was 0.38 ± 0.23 in V1 (mean ± std; 1,358 electrodes with R^2 > 25%), which was significantly smaller than one (Wilcoxon Signed Rank, one-tailed, z = -31.59, p < 0.0001) and similar to the MRI-based values, which had a mean of 0.34 ± 0.19 (6,341 voxels). Likewise, in V4, MUA pRF exponent values were significantly smaller than one (0.33 ± 0.19; z = 11.13, p < 0.0001; n = 165), and comparable to MRI-based values in the same area (0.30 ± 0.16; n = 2,324). The similarity in the values of the pRF exponent indicates that sub-additive spatial summation is a prominent feature in these areas.

The size of the estimated MUA pRFs increased with eccentricity (Figure 9). However, the pRF sizes for two of the V1 arrays in both monkeys were ~3 times smaller than expected when compared to the data from the other arrays. These outlying arrays were located on the posterior-medial side of the surface of V1 in both monkeys where the gray matter is relatively thin (Figure 9A). We therefore suspect that the 1.5 mm long shanks of the Utah arrays were pushed into the white matter, where they picked up activity of thalamic afferents (i.e., the geniculostriate pathway). We therefore excluded these electrodes from the analyses of pRF sizes. The remaining MUA pRF sizes and eccentricities were highly similar to RFs reported in previous

electrophysiology studies at similar eccentricities (Gattass et al., 1987, 1981; Van Essen et al., 1984; Victor et al., 1994). Next, we compared pRFs between the electrophysiological signals and the fMRI BOLD-signal.

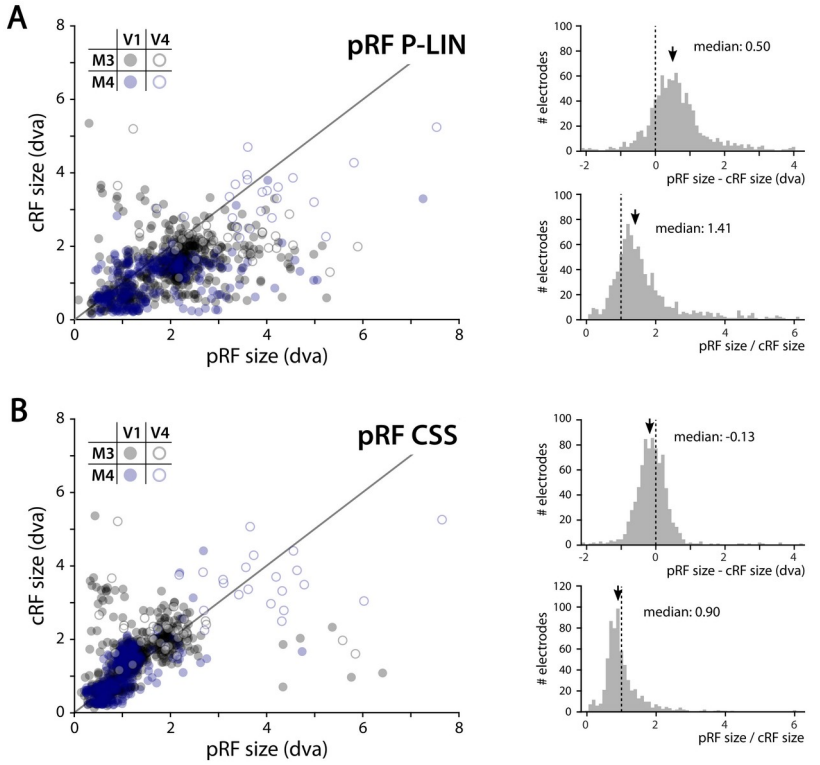

Figure 7. Comparison of MUA pRF sizes with conventionally determined RF (cRF) sizes (moving bar stimulus). Data points represent recording sites of individual animals (black: M3, blue: M4) and brain areas (closed circles: V1, open circles: V4). **(A)** pRF sizes estimated with the P-LIN model (X-axis in left panel) are larger than cRF sizes obtained with a thin moving luminance bar (Y-axis in left panel). The median difference between pRF and cRF sizes across all electrodes (pooled across animals and areas) was 0.50 (IQR: 0.08-0.92) and the median ratio was 1.41 (IQR: 0.99-1.83), as shown in the top and bottom right panels, respectively. **(B)** As in **(A)**, but for pRF sizes estimated with the CSS model, which are slightly smaller than the cRFs (median difference: -0.13, IQR: -0.41-0.14; median ratio 0.90, IQR: 0.67-1.12).

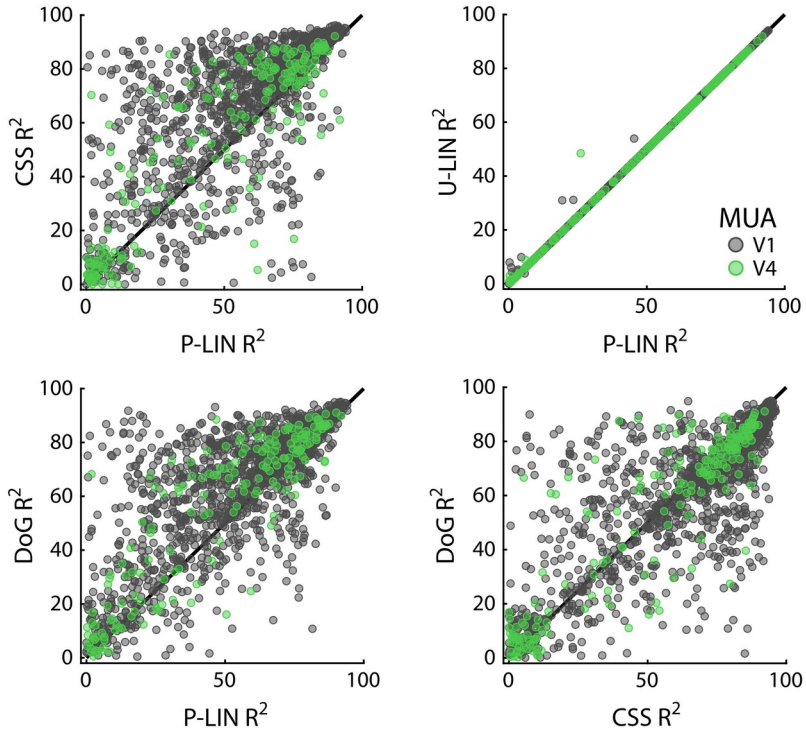

Figure 8. Comparison of MUA-based fit results from the four pRF models. Scatter-plots compare R^2 of pRF models. Each dot represents an electrode (black: V1; green: V4).

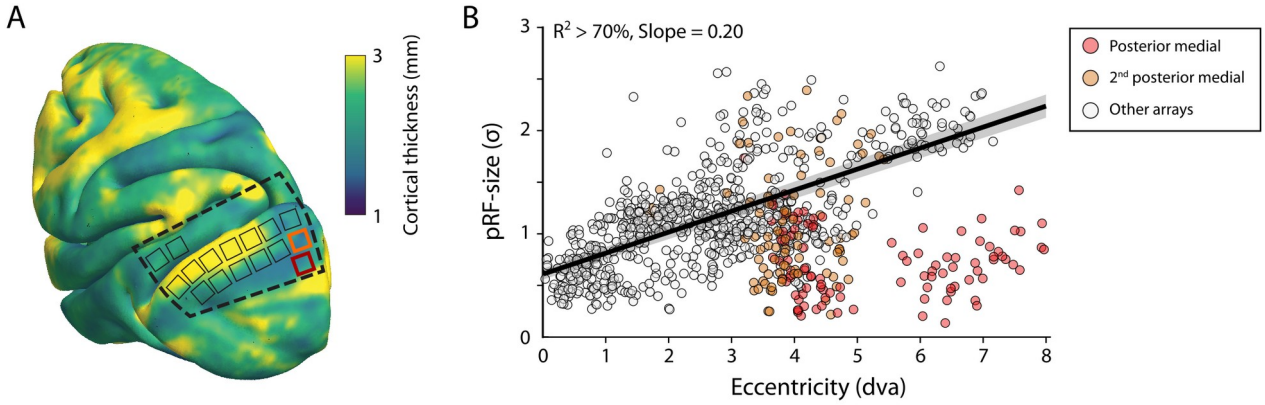

Figure 9. V1 Arrays with outlying pRF sizes. (A) Schematic representation of the location of the craniotomy made during surgery (dashed line) and the implanted electrode arrays (rectangles) depicted on the NMT standard brain. The color map indicates the thickness of the cortical gray matter of the NMT. **(B)** For both monkeys, the estimated pRF sizes of V1 electrode arrays in the posterior medial corner of the craniotomy (red and orange data points correspond to red and orange rectangles in panel **A**) were surprisingly small for their eccentricity, compared to the size-eccentricity relationship seen in the other arrays (gray circles, linear fit with 95% CI as black line and gray area). Given the length of the electrodes (1.5 mm), the typical thickness of the striate cortex, and these small pRF sizes, it is likely that the outlying pRFs do not reflect the tuning of V1 neurons, but that of the geniculostriate pathway in the white matter. The pRF sizes were estimated by the CSS model (recording sites shown have R^2 > 70%).

Local Field Potential pRFs

The LFP was split into five frequency bands: θ (4-8 Hz), α (8-16 Hz), β (16-30 Hz), γ_{low} (30-60 Hz) and γ_{high} (60-120 Hz). We fit the four models to estimate pRFs for each frequency band. The results for γ_{low} and γ_{high} resembled those for the MUA with high R^2-values for a large proportion of the electrodes (especially in V1). The CSS model again outperformed the other models, and we did not observe negative pRFs in these V1 and V4 regions (Supplemental Figures 7 and 8). Electrodes with good MUA-pRF fits usually also had good LFP pRFs, but the opposite was not always true (Supplemental Figure 9). The pRFs in lower frequency bands differed. Whereas θ generally yielded low R^2 values, α and β yielded good fits for a substantial number of electrodes. Interestingly, there were two classes of electrodes in these frequency bands. For the first class the power increased with visual stimulation and CSS model-fits were best. In contrast, the second class of electrodes had negative pRFs, i.e. the stimulus suppressed power (Supplemental Figure 7). Given the few electrodes with good low-frequency LFP-pRFs in V4, we focused our analysis on the positive and negative responses on V1 (the split into positive/negative pRF was based on the parameters of the U-LIN model, Figure 10; Supplemental Figure 10).

We observed a number of remarkable differences between the positive and negative pRFs. First, negative pRFs generally had lower eccentricities than positive pRFs (Figure 10B). Second, negative pRFs were larger than positive pRFs (Figure 10C). Third, there was a systematic difference in the distance from the γ-pRF of the same electrode. Specifically, we calculated a 'separation index' by dividing the distance between the centers of the low and high frequency LFP pRFs by their summed size estimates (SI = Distance/($\sigma_{lf} + \sigma_{hf}$)). A separation index of less than one indicates pRF overlap. For both α and β power, the negative pRFs were farther from the γ-pRFs than the positive pRFs (Figure 10D) and generally shifted in the direction of fixation

(Figure 10E; Supplemental Figures 10E and 11). These results suggest that the positive pRFs represent visually driven activity whereas the negative pRFs signal a form of suppression that is strongest at smaller eccentricities, close to the fixation point. One possible explanation is that the monkeys directed attention to the fixation point, which may have caused a ring of suppression closely surrounding it. Another possibility is that the negative pRFs might be a consequence of small eye movements around the fixation point. The size of α-pRFs did not depend on eccentricity (Figure 10F), whereas the size of β-pRFs increased with eccentricity, although this relation was very weak for positive pRFs (Supplemental Figure 10F).

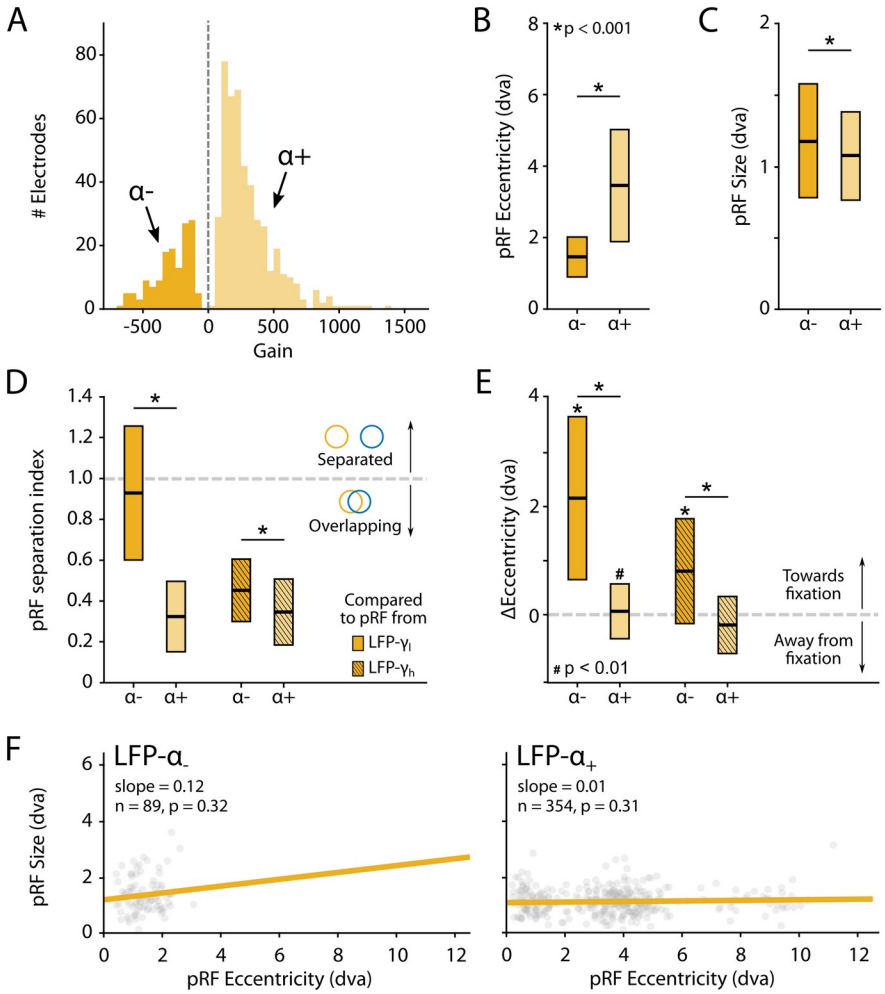

Figure 10. Characteristics of LFP-α pRFs in V1 split by positive and negative gain values. (A) Distribution of gain values for LFP-α pRFs of V1 electrodes estimated with the U-LIN model. Electrodes with positive gain pRFs are classified as α+, electrodes with negative gain pRFs as α-. **(B-C)** PRF eccentricities (**B**) and size (**C**) for α- and α+ electrodes (yellow shades). Colored boxes indicate IQR and the median is shown as a thick horizontal line. Wilcoxon Rank Sum tests were used for comparisons between α- and α+ electrodes. **(D)** Distance between the centers of LFP-α and LFP-γ pRFs from the same electrode, divided by the sum of their respective sizes. Values smaller than one indicate overlapping receptive fields. Non-shaded boxes are comparisons with LFP-γ_{low} pRFs, shaded boxes are comparisons with LFP-γ_{high} pRFs. **(E)** Difference in eccentricity between LFP-γ and LFP-α pRFs from the same electrodes (calculated as Ecc_{γ}-Ecc_{α}). Positive values indicate that LFP-α pRFs are closer to fixation than LFP-γ pRFs. Wilcoxon Signed Rank, one-tailed test (ΔEcc > 0), for individual cases; Wilcoxon Rank Sum test for comparisons between α- and α+ electrodes. See Supplemental Figure 11 for a visualization of the shifts per recording site. **(F)** Eccentricity-size relationship for α- (left) and α+ (right) electrodes. Dots indicate individual electrodes. Supplemental Figure 10 shows the same pattern of results for the LFP-β pRFs.

The pRFs derived from all electrophysiology signals on the same electrode had similar locations, with less than 1 dva between their centers on average (CSS model, Figure 11A). We next analyzed RF sizes, normalizing the size estimates to the MUA-cRF. All LFP-pRFs estimates were larger than MUA-pRFs, and lower frequency LFP-components yielded larger pRFs than the higher frequencies (Figure 11B; we observed the same pattern present in each animal). The pRF exponent was well below one for all LFP-components (V1 and V4 electrodes with $R^2 > 25\%$; Wilcoxon Signed Rank, one-tailed < 1, $p < 0.001$) and smaller at lower frequencies, indicative of stronger compressive spatial summation. We also compared the exponents to those of the MRI-pRFs. The exponent of the MRI was not significantly different from that of γ_{low} in V1, and both γ_{low} and γ_{high} in V4 ($p>0.05$, Figure 11C). Differences between the MRI exponent and those of the other LFP bands were significant (V1: Kruskal-Wallis, H = 505.49, df = 6, $p < 0.0001$; V4: Kruskal-Wallis, H = 21.65, df = 3, $p < 0.001$; Tukey's HSD for multiple comparisons).

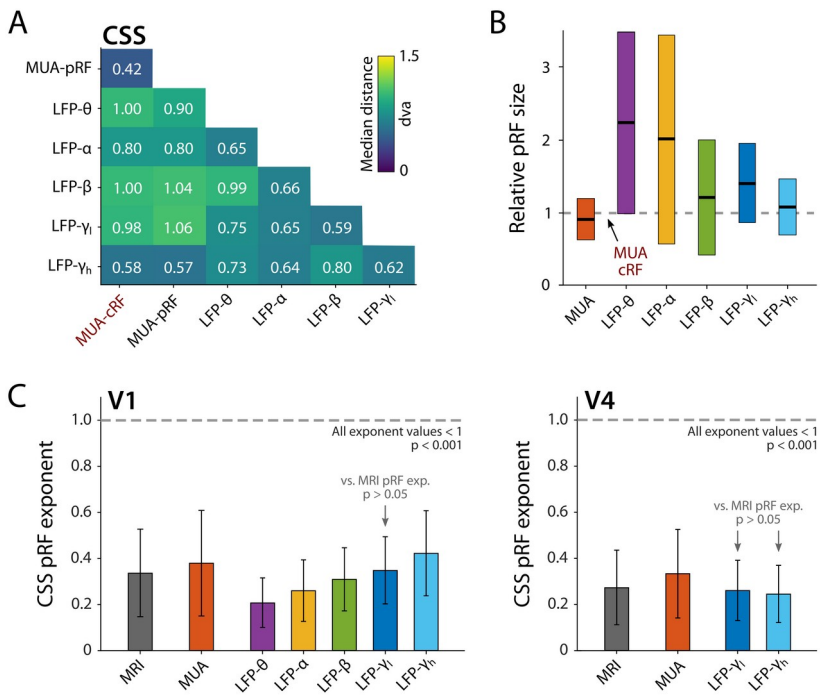

Figure 11. Comparison of pRF location and size of different electrophysiological signals at the same electrode, estimated by the CSS model. (A) Median distance between RF estimates. Electrodes were only included if $R^2 > 25\%$ (MUA, LFP) or SNR > 3 (MUA-cRF). **(B)** RF size for the electrodes of (A), normalized to the MUA-cRF (dashed line). Horizontal lines indicate the median, colored rectangles depict the IQR. **(C)** PRF exponent from the CSS model (indicating nonlinearity of spatial summation). The horizontal dashed line indicates linear summation. The exponent was significantly lower than one for all signals. Gray arrows indicate signals for which the exponent did not significantly differ from that of the MRI pRFs. A similar pattern was present in the electrophysiological data of each animal.

Comparison of pRF eccentricity-size relationship between fMRI and electrophysiology signals

We next compared the eccentricity-size relationship of the electrophysiological signals to that of the BOLD-fMRI pRFs, using Linear Mixed Models (LMM) to evaluate the pRF estimates of the CSS model, separately for V1 and V4 (electrodes with $R^2 > 50\%$ and $R^2 > 5\%$ for MRI). We included voxels for which the pRF was in the lower right visual quadrant where we had electrode coverage. In V1, positive eccentricity-size relationships existed for MRI, MUA, β, γ_{low}, and γ_{high} (Figure 12A). We compared these signals with a single LMM, revealing an interaction between signal type and eccentricity (F = 14.44, df = 4, $p < 0.0001$), which indicated that the slopes differed. We further used pairwise LMMs to compare the slope of the MRI-pRFs to the electrophysiological signals with a significant eccentricity-size relationship. The fMRI eccentricity-size

relationship was similar to that of MUA ($F = 0.38$, $df = 1$, $p = 0.54$), whereas it was significantly different from all LFP signals (β: $F = 7.97$, $df = 1$, $p < 0.01$; γ_{low}, $F = 20.02$, $df = 1$, $p < 0.001$; γ_{high}, $F = 20.05$, $df = 1$, $p < 0.001$) (Figure 12C). We repeated this analysis in V4 (Figure 12B) where we had fewer electrodes. We obtained positive eccentricity-size slopes for MUA, γ_{low}, and γ_{high} but did not obtain fits of sufficient quality for the θ, α and β bands. In contrast to V1, there was no clear difference across these signals ($F = 1.11$, $df = 3$, $p = 0.24$). Pairwise comparisons with the MRI size-eccentricity relationship did not reveal a difference between those for γ_{low} ($F = 0.36$, $df = 1$, $p = 0.55$), γ_{high} ($F = 0.28$, $df = 1$, $p = 0.60$), or MUA ($F = 2.40$, $df = 1$, $p = 0.12$). Because the visual field coverage in V4 differed between the two animals that were used for electrophysiology, we repeated the analysis in both individuals and observed similar results (not shown).

To further investigate the robustness of these results, we repeated the analysis, 1) with the inclusion of either all V1 and V4 voxels or a subset of the voxels in approximately the same anatomical location as the electrode arrays, and 2) by varying the R^2-based inclusion criteria for electrodes and voxels (Supplemental Figure 12). MUA-pRFs in V1 and V4 were generally similar to the BOLD-pRFs, although in V4 γ_{low} and γ_{high} also approximated the fMRI results in some of the comparisons.

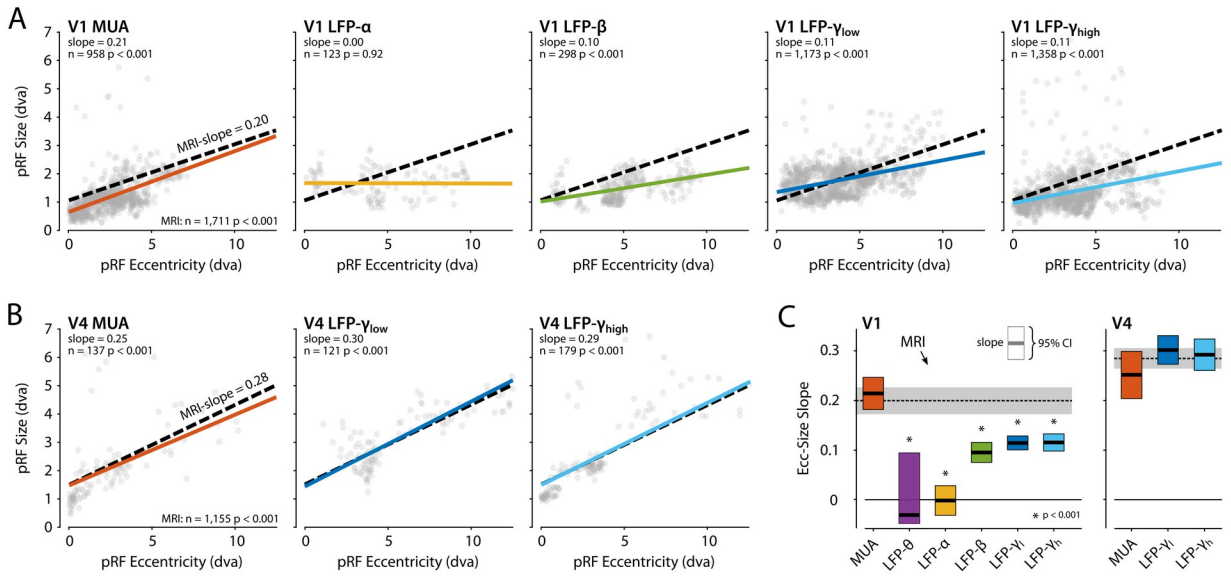

Figure 12. Eccentricity-size relationship for pRFs across signal types. (A) The pRF size-eccentricity relation for V1 electrodes (CSS model, $R^2 > 50\%$). Dots are individual electrodes, colored lines represent the slope of the eccentricity-size relationship. The dashed black line represents the relationship for V1 MRI voxels with a pRF in the lower right visual quadrant and an $R^2 > 5\%$. We only included signals with > 25 electrodes meeting the R^2 threshold. **(B)** Same as in (A), but now for the V4 electrodes and voxels. **(C)** Eccentricity-size slopes (left: V1, right: V4). The dashed line represents the slope for MRI-based pRFs with the 95% confidence interval depicted in gray shading. Colored rectangles indicate the 95% confidence intervals for the electrophysiological signals and the horizontal black line the slope estimate. The lower bound of the 95% confidence interval of the LFP-θ is not visible. Asterisks indicate significant difference with the size-eccentricity relation of the MRI-based pRFs.

375 # Discussion

376 The current study conducted a systematic comparison of pRFs obtained with fMRI and electrophysiological
377 recordings in V1 and V4 of awake behaving macaque monkeys. Within the same species, we fit several pRF
378 models to seven different signal types (BOLD, MUA, and the power in five LFP frequency bands) to gain
379 insight into the neuronal basis of MRI-BOLD pRF measurements (Wandell and Winawer, 2015). Our results
380 demonstrate retinotopic tuning in many brain regions and the presence of negative pRFs in areas of the DMN.
381 We found that subadditive spatial summation is a prominent feature of many measures of brain activity.
382 Furthermore, the results establish a clear relationship between BOLD-pRFs and electrophysiologically
383 determined pRFs, with MUA-pRFs being most similar to BOLD-pRFs (as discussed below).

384 **Cortical and subcortical retinotopic tuning of the BOLD signal**

385 Retinotopic information was present in occipital, temporal, parietal, and frontal cortex as well as in a
386 subcortical areas. We could differentiate the lateral geniculate nucleus (LGN) and pulvinar from their
387 surrounding areas based on their higher R^2. Retinotopic maps in the LGN were roughly in line with previously
388 published retinotopic organization of the macaque LGN (Erwin et al., 1999), but they comprised few voxels
389 and the variability across animals prohibited detailed inferences. In the pulvinar, the organization of the
390 retinotopic information was even more variable across animals. In humans, subcortical retinotopic maps have
391 been observed in LGN, pulvinar, superior colliculus (SC), thalamic reticular nucleus (TRN), and substantia
392 nigra (SN) (Cotton and Smith, 2007; DeSimone et al., 2015; Schneider et al., 2004). Here, we also observed
393 voxels with pRFs located lateral, and medial to the pulvinar, but more targeted investigations are necessary for
394 detailed individual-subject segmentation of the thalamus (DeSimone et al., 2015; Tani et al., 2011).

395 We obtained good pRF fits in the occipital, temporal and parietal cortical areas, regions for which previous
396 studies demonstrated retinotopic organization with phase-encoded retinotopic mapping (Arcaro et al., 2011;
397 Janssens et al., 2014; Kolster et al., 2014, 2010, 2009; Patel et al., 2010). Despite the fact that checkerboard
398 stimuli may not be ideal for the activation of frontal areas, which are better driven by more complex stimuli
399 (Janssens et al., 2014; Saygin and Sereno, 2008), we also observed retinotopy in several frontal areas,
400 including the insula, cingulate cortex, frontal eye fields (FEF, area 8), orbitofrontal cortex, ventromedial
401 prefrontal cortex and dorsolateral prefrontal cortex. These areas are thought to be involved in visual
402 processing and visual attention. Retinotopic maps have previously been reported in the cerebellum in humans
403 (van Es et al., 2019). We did not detect such maps, likely because of a lower SNR in the cerebellum due to
404 lower field strength, a less optimal coil placement, and the sphinx position of the monkeys.

405 **Negative pRFs**

406 We observed negative pRFs in the MRI data and in the low frequency LFP, but they were of a different
407 nature. We identified two classes of negative pRFs in the MRI data. Negative pRFs in the visual cortex were

usually accompanied by positive responses at peripheral visual field locations, close the boundaries of the visual display. Similar negative visual BOLD responses have been reported in human visual cortex (Smith et al., 2004) and are presumably caused by surround suppression (Allman et al., 1985; Cavanaugh et al., 2002; Hubel and Wiesel, 1962; Knierim and van Essen, 1992). We found a second class of negative pRFs around the lateral sulcus, in the medial occipital parietal cortex, and at the superior border of the superior temporal sulcus in the lateral occipital parietal cortex, all areas previously implicated in the monkey's DMN (Mantini et al., 2011). A similar retinotopy of negative responses was recently found in the human DMN (Szinte and Knapen, 2019). The retinotopy of nodes of the DMN in humans and monkeys implies a sensory-based organization of this part of the DMN, which could play role in visual cognition (Arsenault et al., 2018).

Negative pRFs were also observed for a subset of the electrodes in the α and β range of the LFP, although pRF fits were generally of lower quality than those for the γ-LFP or MUA signals. It is conceivable that these negative pRFS reflect shifts of attention, which are known to modulate α and β power (Griffiths et al., 2019; Siegel et al., 2008; Womelsdorf and Fries, 2007; Worden et al., 2000). In accordance with this idea, negative α/β pRFs were larger than their positive counterparts, and shifted towards the fixation point. Future studies are needed for a closer examination of this phenomenon.

The relation between BOLD-based pRFs and electrophysiologically determined pRFs

We compared BOLD-based pRFs to electrophysiological measures in terms of their spatial summation characteristics, size, and the relationship between eccentricity and size (Amano et al., 2009; Dumoulin and Wandell, 2008; Felleman and Van Essen, 1987; Gattass et al., 2005; Kay et al., 2013; Larsson and Heeger, 2006; Van Essen et al., 1984; Victor et al., 1994). Eye-movements can have an effect on the pRF size estimates and it is therefore important to note that 1) we only included data from recordings where the animals maintained a high fixation performance (IQR-span of the horizontal and vertical eye position, M1: 0.23, 0.34 dva; M2: 0.36, 0.49 dva; M3: 0.18, 0.38 dva; M4: 0.37, 0.60 dva), and 2) we averaged across multiple stimulus presentations to obtain robust response profiles. Hence, variations in eye position can have had only minor effects on the present results.

Compressive spatial summation

The CSS pRF model includes nonlinear spatial summation (Kay et al., 2013). Previous studies observed sub-additive spatial summation, also known as spatial compression, throughout the human visual cortex in BOLD-based pRFs, with stronger compression in higher visual areas than in V1 (Kay et al., 2013; Winawer et al., 2013). In the present study, spatial compression was present in subcortical and cortical areas with good BOLD-pRF fits, indicating that it is a widespread, if not universal, characteristic of the primate visual system. The strength of compression did not differ much across areas and it was similar to that in human V1. For the MUA data, the CSS model estimated pRF sizes that were very similar to RF size estimates derived from conventional methods that use moving luminance bars, whereas the P-LIN model systematically returned

larger pRF estimates. This difference might indicate that spatial compression indeed better captures the neuronal RF properties, at least in V1 and V4.

In human iEEG recordings, spatial compression in the broadband iEEG signal was reported to be similar in strength to that of the BOLD signal (Winawer et al., 2013). We also observed compressive spatial summation in both the MUA-pRFs and in all frequency bands of the LFP, and the pRF exponent tended to be smaller for lower-frequency components, indicative of stronger compression. The lower frequencies also exhibited stronger suppression than the BOLD signal. In contrast, the pRF exponent of MUA and γ_{low} was similar to that of BOLD fMRI in both V1 and V4, but in V1 the exponent for γ_{high} was larger. Hence, MUA and γ_{low} were the two electrophysiological markers for which spatial compression resembled that of BOLD fMRI most.

PRF size and the eccentricity-size relationship

As expected, pRFs were larger at higher eccentricities, with a larger slope in higher visual cortical areas. The pRF sizes and the eccentricity-size relationships that we found in visual cortex were in line with previous results from human and monkey neuroimaging studies (Amano et al., 2009; DeSimone et al., 2015; Dumoulin and Wandell, 2008; Kay et al., 2013; Keliris et al., 2019; Kolster et al., 2014, 2010; Welbourne et al., 2018; Zhu and Vanduffel, 2019; Zuiderbaan et al., 2012). Furthermore, the results are in keeping with previous electrophysiological recordings of single units and MUA in early visual areas such as V1 (Gattass et al., 1987, 1981; Van Essen et al., 1984; Victor et al., 1994), V2 (Burkhalter and Van Essen, 1986; Gattass et al., 1981; Rosa et al., 1988), V3 (Burkhalter and Van Essen, 1986; Felleman and Van Essen, 1987; Newsome et al., 1986; Rosa et al., 2000), and V4 (Gattass et al., 1988). Finally, they also match the results of human electrophysiology with subdural electrodes (Harvey et al., 2013; Yoshor et al., 2007).

The spatial scope of fMRI-BOLD, MUA, and LFP

The spatial scale of recorded neural signals depends both on the nature of the signal and the recording method. For extracellular electrophysiology recordings, the impedance and size of an electrode determine its sensitivity for single- or multi-unit spiking activity. This relationship is complex (Viswam et al., 2019; Ward et al., 2009), but high impedance (~1 MΩ) electrodes are generally better suited for the detection of spiking activity, with smaller contact sites and higher impedance thought to sample from smaller neural populations and being more likely to pick up single-neuron activity. The spatial range of the MUA signal is ~140 µm (Buzsáki, 2004). Electrode impedance, size and shape are less important for LFP recordings, at least within commonly used ranges (Nelson and Pouget, 2010; Viswam et al., 2019). The spatial extent of the LFP signal is a topic of ongoing debate (Kajikawa and Schroeder, 2011) with some authors estimating it as low as 120-250 µm in visual cortex (Katzner et al., 2009; Xing et al., 2009), while others suggest it may stretch up to several millimeters (Berens et al., 2008; Katzner et al., 2009; Kreiman et al., 2006), and may even be detected more than a centimeter away from the source (Kajikawa and Schroeder, 2011). The hypothesis that low-frequency components of the LFP have a larger spatial reach than high-frequency components is supported by computational modeling (Łęski et al., 2013), although it has also been challenged (Dubey and Ray, 2016).

Yet, the exact origin of the LFP and its relationship to spiking remains to be completely understood (Einevoll et al., 2013).

Given the larger spatial spread of the LFP compared to MUA, one would expect pRFs based on LFPs to be larger than those based on MUA. This is indeed what we found. The size of LFP-pRFs furthermore depended on the frequency component of the LFP, with lower frequencies yielding larger pRFs, suggesting a frequency-dependent spread of visual information in the LFP signal. In fMRI, there is a trade-off between spatial and temporal resolution. While higher magnetic field strengths and specialized acquisition methods are continuously increasing spatiotemporal resolution, studies with voxel sizes on the order of 1-2 mm isotropic and a repetition time of 2-3 seconds at 3T field-strengths are still common. Due to the complex relationship between the hemodynamic BOLD signal and the underlying neural activity, it is difficult to predict its stimulus-sensitivity from neuroimaging parameters such as voxel size. Nonetheless, a comparison of the eccentricity-size relationship between MRI and electrophysiology in V1 revealed that the BOLD-based pRFs resembled MUA in V1 and V4. In V4, however, the BOLD slope was also very similar to that of the LFP gamma power (Supplementary Figure 12). One possible reason for this difference between areas is that V4 is smaller and more heterogeneous (Kolster et al., 2014; Zhu and Vanduffel, 2019) than V1. A V4 voxel therefore samples from a neuronal population with more heterogeneous spatial tuning than an equally sized V1 voxel and may therefore reflect the activity of a larger population of neurons, which is better approximated by gamma power. Other factors that might play a role are potential differences in the quality of the recorded signal across areas, or partial volume effects that are likely to be more prevalent in V4 than in V1.

Conclusions

Our comparison of fMRI with large-scale neurophysiological recordings in visual cortex revealed that pRFs derived from the BOLD signal resemble MUA RFs. Sub-additive spatial summation is a general feature of many brain areas and occurs for BOLD, MUA and LFP. We observed negative pRFs in the monkey default mode network and as part of center-surround organization of pRFs in early visual areas. The spatial compression and the eccentricity-size relationship of BOLD resembles that of MUA, but also bears a resemblance to gamma power. We conclude that BOLD pRFs accurately represent the spatial tuning of the underlying neuronal populations.

Materials and Methods

Subject details

Four male macaques (*Macaca mulatta;* 7-12 kg, 5-8 years old) participated in this study. Animal care and experimental procedures were in accordance with the ILAR's Guide for the Care and Use of Laboratory Animals, the European legislation (Directive 2010/63/EU) and approved by the institutional animal care and

use committee of the Royal Netherlands Academy of Arts and Sciences and the Central Authority for Scientific Procedures on Animals (CCD) in the Netherlands (License numbers AVD8010020173789 and AVD8010020171046). The animals were socially housed in an enriched specialized primate facility with natural daylight, controlled temperature and humidity, and fed with standard primate chow, supplemented with raisins, fresh fruits, and vegetables. Their access to fluid was controlled, according to a carefully designed regime for fluid uptake. During weekdays the animals received diluted fruit juice in the experimental set-up. We ensured that the animals drank sufficient fluid in the set-up and received extra fluid after experimental sessions if needed. On the weekends, animals received at least 700 ml of water in the home-cage. The animals were regularly checked by veterinary staff and animal caretakers and their weight and general appearance were recorded in an electronic logbook on a daily basis during fluid-control periods.

Surgical procedures

Two animals (M1 & M2) participated in the MRI experiments and were implanted with an MRI-compatible plastic (PEEK) head-post, fixed to the skull with ceramic bone screws and acrylic (Farivar and Vanduffel, 2014; Vanduffel et al., 2001). Anesthetics, analgesics and monitoring procedures were similar to previous surgical procedures in our laboratory and are described in detail elsewhere (Klink et al., 2017; Poort et al., 2012; Supèr and Roelfsema, 2005). Two other animals (M3 & M4) participated in the electrophysiology experiments. They were implanted with a custom 3D-printed titanium head-post that was designed in-house based on a CT-scan of the skull, aligned to a T1-weighted anatomical MRI-scan of the brain (Chen et al., 2020, 2017). The titanium head-post was attached to the skull with titanium bone-screws and the skin was closed around the implant without the use of any acrylic. In a second surgery, each animal was additionally implanted with a total of 1,024 electrodes in 16 Utah electrode arrays (Blackrock Microsystems) in their visual cortices (14 arrays in V1, 2 arrays in V4; Figure 1B). Each array contained an 8-by-8 grid of 64 iridium oxide electrodes with a length of 1.5 mm spaced at a distance of 400 μm from each other. Pre-implantation electrode impedances ranged from 6 to 12 kΩ. A custom designed 1,024-channel pedestal was attached to the skull with titanium bone screws and the skin was closed around it. More details on the surgical procedures have been published elsewhere (Chen et al., 2020, 2017).

Visual stimuli and procedures

In the MRI experiment, animals were head-fixed, sitting in the sphinx position (Farivar and Vanduffel, 2014; Vanduffel et al., 2001), and viewing a 32” screen (1920×1080 pixels, 100 Hz) (Cambridge Research Systems) at the end of the bore, 130 cm away. Population receptive fields were measured using conventional moving bar stimuli that traversed the screen in eight different directions behind a large virtual circular aperture (Figure 1). The borders of this virtual aperture were invisible, because both the foreground and background had the same gray level (22.3 cd/m^2) (Dumoulin and Wandell, 2008). In the MRI experiments, the bar sweep spanned 16° (diameter) in 20 steps (Dumoulin and Wandell, 2008). The moving bars were 2° wide and contained a

checkerboard pattern (100% contrast; 0.5° checkers; luminance of white checkers: 106.8 cd/m^2; luminance of black checkers: 0.2 cd/m^2) that moved parallel to the bar's orientation. Each bar position was on the screen for 2.5 s (1 TR) making one full bar sweep last 50 s. Bar sweep series (all directions presented once) were preceded and followed by 37.5 s (15 TRs) of neutral gray background. Each horizontal or vertical bar sweep was followed by a neutral gray background period of 25 s. The order of the bar sweep directions was 270°, 315°, 180°, 225°, 90°, 135°, 0°, 45° on most runs, but for one animal we inverted the directions to 90°, 135°, 0°, 45°, 270°, 315°, 180°, 225° on some runs to compensate for the animal's tendency to fall asleep near the end of runs. We included data from 8 scanning sessions for monkey M1 (34 runs, 268 bar sweeps) and 10 sessions for monkey M2 (66 runs, 406 bar sweeps). During stimulus presentation the animals received fluid rewards (Crist Instruments, Hagerstown, MD) for maintaining fixation within a circular fixation window with a diameter of 2°, centered on a 0.15° red fixation dot, surrounded by a 0.75° (diameter) aperture of neutral gray background color. In the electrophysiology experiments, the stimulus and task were very similar, but bar sweeps now spanned 28°, which was possible because the animals were closer to the monitor (luminance values of this monitor were black: 0 cd/m^2; white: 92.1 cd/m^2, neutral gray: 14.8 cd/m^2). Bars traveled along this path in 30 steps of 500 ms, and the neutral gray luminance intervals were reduced to 2.5 s due to the much faster neuronal responses (compared to the BOLD signal). The fixation window in the electrophysiology experiments was slightly smaller with a diameter of 1.5°. In the MRI experiment, eye-position and pupil diameter were tracked with an MRI-compatible infrared eye-tracking system at 120 Hz (ISCAN ETL-200). Hand positions were also monitored using fiber optic amplifiers (Omron E3X-NH) and optic fibers. To reduce body movement-related imaging artifacts, the animals were trained to maintain their hands inside a response-box by making reward delivery contingent on both eye and hand position. In the electrophysiology experiments, animals were head-fixed in a conventional vertical primate chair and viewed a 21" CRT monitor (1024×768, 85 Hz) at a distance of 64 cm while their eye-position and pupil diameters were tracked at 230 Hz using an infrared eye-tracker (TREC ET-49B, Thomas Recording GmbH).

MRI acquisition

MR-imaging was performed in a standard Philips Ingenia 3.0 T horizontal bore full-body scanner (Spinoza Center for Neuroimaging, Amsterdam, the Netherlands). We used a custom-built 8-channel phased array receive coil system (Ekstrom et al., 2008; Kolster et al., 2009) (KU Leuven) and the scanner's full-body transmit coil. Functional images were obtained using a gradient-echo T2* echo-planar sequence (44 horizontal slices, in-plane 72 × 68 matrix, TR = 2500 ms, TE = 20 ms, flip angle = 77.2°, 1.25×1.25×1.25 mm isotropic voxels, SENSE-factor of 2 in the AP direction, and phase-encoding in the AP direction).

fMRI preprocessing

All fMRI data was preprocessed with a custom-written Nipype pipeline that we have made available online (https://github.com/visionandcognition/NHP-BIDS). In short, MRI scans were exported from the scanner as

DICOM images and converted to NIFTI files with the dcm2niix tool (Li et al., 2016). The volumes were then re-oriented to correct for the animal being in the sphinx position and resampled to 1 mm^3 isotropic voxels. The resulting images were re-aligned using a non-rigid slice-by-slice registration algorithm based on AFNI tools (Cox, 1996) followed by an FSL-based motion correction procedure MCFLIRT (Jenkinson et al., 2002). Functional volumes were linearly aligned to the individual high-resolution anatomical volumes, which were in turn non-linearly registered to the NMT standard space (Seidlitz et al., 2018). Preprocessed data was further processed with a combination of custom written Matlab (Mathworks, Natick, MA) and shell scripts (https://gin.g-node.org/ChrisKlink/NHP-PRF). BOLD time-courses for each voxel were normalized to percentage signal change and averaged across runs (or parts of runs) for which fixation was maintained at 80% of the time or more. We averaged odd and even runs separately to allow for a cross-validation approach in the evaluation of the pRF model fits. Anatomical regions of interest (ROI's) were defined based on a probabilistic atlas (Reveley et al., 2017; Seidlitz et al., 2018) and refined using individual retinotopic maps.

Post-fit comparisons across pRF-models, HRFs, and ROIs were performed in Matlab based on the volumetric results. For visualization of the fMRI data, volumetric results were also projected to the individual cortical surfaces. To create these surfaces, we averaged multiple anatomical scans (T1-weighted, 3D-FFE, TE = 6 ms, TR = 13 ms, TI = 900 ms, flip angle = 8°, 100 horizontal slices, in-plane 224 × 224 matrix, 0.6×0.6×0.6 mm isotropic voxels, and phase-encoding in the AP direction) and processed the result with customized tools based on Freesurfer (Fischl, 2012) and Pycortex (Gao et al., 2015) that were adjusted to handle our NHP data. These tools and their documentation can be found at https://github.com/VisionandCognition/NHP-Freesurfer and https://github.com/VisionandCognition/NHP-pycortex respectively (Messinger et al., 2021).

Electrophysiology acquisition

Neuronal activity was acquired from 1,024 channels simultaneously at a 30 kHz sampling rate. The 1,024-channel pedestal was connected to eight 128-channel CerePlex M head-stages through an electronic interface board. Each head-stage processed signals from two 64-channel electrode arrays with a 0.3-7,500 Hz analog filter at unity gain (i.e., no amplification). After analog-to-digital conversion, the signal from each head-stage was sent to a 128-channel Digital Hub (Blackrock Microsystems) where it was converted into an optical output signal and sent to a 128-channel Neural Signal Processor (NSP, Blackrock Microsystems) for storage and further processing. The eight NSPs were controlled with eight simultaneously running instances of the Blackrock Central Software Suite (Blackrock Microsystems) distributed over two computers (four instances each) (Chen et al., 2020).

Electrophysiology data preprocessing

The neuronal signal that was acquired using different software instances was temporally aligned using common TTL pulses sent by the stimulus computer. The data were then separated in 1) envelope multi-unit activity (MUA), and 2) broadband local field potential (LFP). MUA represents the spiking activity of a local

population of neurons around the electrode (Cohen and Maunsell, 2009; Palmer et al., 2007; Supèr and Roelfsema, 2005). To extract MUA, we amplified the raw neuronal signal, band-pass filtered it between 500 Hz and 9 kHz, full-wave rectified it, and applied a low-pass filter of 200 Hz. The resulting time-series were down-sampled to 1 kHz. We subtracted the baseline MUA activity in a 1,000 ms prestimulus time-window. Baseline-corrected MUA responses were then averaged, first across runs and then within a 50-500 ms time window for each stimulus position. The broadband LFP signal was generated by low-pass filtering the raw signal at 150 Hz and down-sampling it to 500 Hz. The LFP signal was further processed with a multi-taper method using the Chronux toolbox (Bokil et al., 2010). Power spectra were calculated in a 500 ms moving window (step-size 50 ms), using a time bandwidth product of 5 and 9 tapers. LFP power was averaged within five distinct frequency bands: 4-8 Hz (Theta), 8-16 Hz (Alpha), 16-30 Hz (Beta), 30-60 Hz (low Gamma), and 60-120 Hz (high Gamma). Baseline power in a 1,000 ms pre-stimulus period was subtracted and the power for each recording site was averaged across runs, within a 50-500 ms time window during each stimulus position.

Population receptive fields models and fitting procedure

We fit four pRF-models to all the data (voxels and electrode channels) using a customized version of the analyzePRF toolbox (Kay et al., 2013) for Matlab. In the fitting procedure, the stimuli were spatially down-sampled to a resolution of 10 pixels per dva and converted to 'effective stimuli', consisting of binary representations that encode stimulus position. Response predictions were calculated as the product of the effective stimulus and the pRF shape (Eq. 1). This method also yields a prediction for pRFs that are only partially stimulated, and the best fitting pRF can have a center location outside of the stimulus aperture. Because pRF estimates are generally more reliable for pRF that are strongly driven by a visual stimulus, we include indications of the directly stimulated visual field in our figures. The four pRF-models differed in the pRF shape. Linear models (Eq. 1-3) describe a single isotropic 2D Gaussian-shaped pRF and assume linear spatial summation across the visual field (Dumoulin and Wandell, 2008). We implemented two linear model versions. For the first model, responses were constrained to be positively related to the visual stimuli (P-LIN). A second version lacked this constraint and also allowed negative responses, i.e. stimulus-driven activity reductions (U-LIN). Negative BOLD responses have been demonstrated in some brain areas (Shmuel et al., 2006; Szinte and Knapen, 2019). The Non-linear Spatial Summation model (Kay et al., 2013) expands the linear model by capturing non-linear summation of signals across the visual field. It has previously been shown that the value of the exponent is generally smaller than one in human visual cortex, indicating sub-additive spatial summation or compressive spatial summation (Kay et al., 2013). This model is therefore generally referred to as the compressive spatial summation (CSS) model. Because the pRF size and static non-linearity interact in the non-linear model, the pRF size is defined as the standard deviation of the predicted Gaussian response profile to a point stimulus for all models (Eq. 3) (Kay et al., 2013). The mathematical descriptions of the linear and non-linear pRF-models are in Equations 1-3, where $Resp_{\text{pred}}$ indicates the predicted response, g is a gain factor to scale the response, $S(x,y)$ is the effective stimulus, $G(x,y)$ the Gaussian pRF profile, and n the exponent that determines the static spatial non-linearity. For the P-LIN model, the gain

g was constrained to positive values, while for the U-LIN model, gain values could be negative as well. Negative gain factors imply stimulus-induced reductions of activity. In both linear models, the exponent n was fixed to be one. In the definition of the Gaussian, (x_0,y_0) defines the center and σ the standard deviation of the pRF.

Linear and Non-linear spatial summation pRF models

[1] $$Resp_{\text{pred}} = g \cdot \left[\sum_{x,y} S(x,y)\, G(x,y) \right]^n, \begin{matrix} \text{P-LIN, U-LIN}: n=1 \\ \text{P-LIN, CSS}: g>0 \end{matrix}$$

[2] $$G(x,y) = e^{\frac{-(x-x_0)^2+(y-y_0)^2}{2\sigma^2}}$$

[3] $$pRF_{\text{size}} = \frac{\sigma}{\sqrt{n}}$$

The Difference-of-Gaussians (DoG) model uses a standard linear Gaussian (G_1 in Eq. 4) to describe the excitatory center of a pRF and subtracts a second Gaussian profile (G_2) to model an inhibitory surround component (Zuiderbaan et al., 2012). This second Gaussian is by definition broader than the one describing the center. The size σ_2 and amplitude a of the surround Gaussian are additional parameters (Eq. 4-6).

Difference-of-Gaussians pRF model

[4] $$Resp_{\text{pred}} = g \cdot \left[\sum_{x,y} S(x,y) \left(G_1(x,y) - a \cdot G_2(x,y) \right) \right]^n$$

[5] $$G_1(x,y) = e^{\frac{-(x-x_0)^2+(y-y_0)^2}{2(\sigma_1)^2}}, G_2(x,y) = e^{\frac{-(x-x_0)^2+(y-y_0)^2}{2(\sigma_2)^2}}; \sigma_2 > \sigma_1$$

[6] $$pRF_{\text{center-size}} = \sigma_1, pRF_{\text{surr-size}} = \sigma_2$$

The models assume a near-instantaneous link between the stimulus and the response dynamics, which holds for the electrophysiological signals. For these signals, the stimulus changes position every 500 ms, much slower than the onset or decay of activity. The BOLD-response is much slower than the speed with which the stimulus traverses the screen in the fMRI experiments (2,500 ms per position). We therefore convolved the predicted response with a hemodynamic response function (HRF) at a resolution of 1.25 seconds per sample (twice the acquisition rate of TR = 2.5s). We used both a canonical human HRF and a standard monkey HRF that we derived from separate scanning sessions (Supplemental Figure 13). In short, we presented the animals with brief (0.1 s) full contrast and fullscreen checkerboard stimuli. We then used FMRIB's Linear Optimal

Basis Sets (FLOBS) (Woolrich et al., 2004) toolkit from the FSL software package to estimate the relative contributions of a set of basis functions for those voxels in the primary visual cortex that were activated by the stimulus. We then calculated a single weighted average HRF function based on these basis functions and used it as the standard monkey HRF. The monkey HRF was narrower than the canonical human HRF. It had a faster time-to-peak (4.2 s vs. 4.8 s) and peak-to-fall time (6.2 s vs. 12.6 s). The fits with the monkey HRF were slightly better, especially in the lower visual areas (Supplemental Figure 13). However, size and location estimates were highly similar for the two HRFs for all models, and we only report results from model-fits based on the monkey HRF.

Model-fitting was performed on a cluster-computer (LISA, SURFsara) using nonlinear optimization (MATLAB Optimization Toolbox). The accuracy of the different model-fits was quantified as the cross-validated percentage of variance (R^2) explained of the BOLD-response (Eq. 7: *DATA*) by the model prediction (Eq, 7: *MODEL*). For cross-validation, we divided the data into two non-overlapping sets (odd and even runs) and tested the prediction of a model that was fit one data-set against the time-series of the other data-set and vice-versa. This yielded two R^2 values per voxel or electrode that were averaged. The cross-validated comparison of model performance is valid for models with different numbers of parameters and prevents over-fitting. Fit-results are available as voxel-based maps warped to the NMT template space on Neurovault.org (Fox et al., 2021; Gorgolewski et al., 2015) at https://identifiers.org/neurovault.collection:8082.

Model accuracy

[7] $$R^2 = 100 \times \left[1 - \frac{\sum (MODEL - DATA)^2}{\sum DATA^2} \right]$$

Comparison of pRF (& cRF) estimates

After fitting the pRF models to all voxels and recording sites we compared the pRF estimates both within and across recording modalities. We pooled voxels and recording sites across subjects and used non-parametric statistical tests (Wilcoxon Signed Rank, Wilcoxon Rank Sum, or Kruskal-Wallis) with post-hoc Tukey's HSD tests to correct for multiple comparisons. For the fMRI data we compared R^2 across models and hemodynamic response functions. We constructed retinotopic maps using the best pRF model and HRF and investigated the relationship between pRF eccentricity and size for a subset of ROI's with good model fits ($R^2 > 5\%$). For the electrophysiological data, we compared model accuracy and pRF estimates across MUA and LFP components to unravel to which extent retinotopic information is available in the different neuronal signals. We also compared the pRF estimates to a more conventional RF mapping technique for MUA based on responses to thin, moving bar stimuli (cRF). For recording sites with a signal-to-noise ratio (SNR) larger than three (i.e.,

visual responses that were more than three times larger than the standard deviation of the spontaneous activity), we fitted a Gaussian to the averaged MUA traces and determined the onset and offset of the visual response as the mean of this Gaussian plus or minus its standard deviation (SD). Horizontal and vertical receptive field boundaries were then derived from the onset and offset times for stimuli moving in opposite directions (Supèr and Roelfsema, 2005). Receptive field centers were defined as the midpoint between the horizontal and vertical borders. For comparison with the pRFs, we calculated RF sizes as half the diagonal of the rectangular area between the horizontal and vertical cRF borders ($cRF_{sz} = \sqrt{(width^2 + height^2)}/2$). This measure approximates the RF radius based on the SD of a Gaussian response profile, and can be directly compared to the sigma estimated by pRF-models (Figure 7). It is smaller than cRF sizes typically reported in electrophysiological studies, because neurons are activated by stimuli farther than one SD from their RF center (our lab usually defines cRF diameter as 3.3*SD).

To compare pRFs based on fMRI BOLD and electrophysiology, we combined data from individual animals to create one pool of BOLD-based voxel pRFs and six pools of electrophysiology-based electrode pRFs (MUA, and the different frequency bands of the LFP) for V1 and V4 data. We compared the relationship between RF eccentricity and size with a set of Linear Mixed Models (LMMs). We first tested for a correlation between eccentricity and size for the different signal types. Signal types with a significant correlation were subsequently tested together in a single LMM to determine whether the eccentricity-size relationship differed between signal types (interaction SIGNAL × ECC). Finally, we compared electrophysiological signals with the MRI results. For this analysis, we only selected V1 and V4 voxels with pRFs falling within the eccentricity range of the electrode arrays and voxels and electrodes with a fit accuracy above a predetermined threshold (fMRI threshold: $R^2 > 5\%$, electrophysiology threshold: $R^2 > 50\%$). To test the robustness of the results for this analysis, we repeated it with different combinations of criteria for initial voxel inclusion (i.e., including only voxels that roughly correspond to the location of the electrode arrays, or including all V1 and V4 voxels) and fit quality (fMRI threshold: $R^2 > 5\%$ or 10%, electrophysiology threshold: $R^2 > 25\%$ or 50%; Supplemental Figure 12).

Data and code availability

All data, experiment code, and analysis code used for this study have been made freely available at GIN (https://doi.org/10.12751/g-node.p8ypgv).

Acknowledgments

We thank Jonathan Williford for his contributions to the fMRI preprocessing pipeline; Pieter Buur, Wietske van der Zwaag, Diederick Stoffers, and the Laboratory of Neuro- and Psychophysiology of KU Leuven for technical assistance in setting up the non-human primate MR infrastructure; Kor Brandsma, Anneke Ditewig, and Lex Beekman for animal care and biotechnical assistance; Feng Wang for help with electrophysiology

data collection; Chris van der Togt for help with data management; and Tomas Knapen and Serge Dumoulin for fruitful discussion and comments on an earlier version of the manuscript. This work was supported by NWO (Crossover Program 17619 “INTENSE”; STW-Perspectief P15-42 “NESTOR”; VENI 451.13.023), the European Union FP7 (ERC 339490 “Cortic_al_gorithms”), the Human Brain Project (agreements 720270 and 785907, “Human Brain Project SGA1 and SGA2”), and the Friends Foundation of the Netherlands Institute for Neuroscience.

Author contributions (CRediT)

P.C. Klink: Conceptualization, Methodology, Software, Investigation, Formal Analysis, Resources, Data Curation, Writing – Original Draft Preparation, Writing – Review & Editing, Visualization, Project Administration, Funding Acquisition.

X. Chen: Investigation, Formal Analysis, Writing – Review & Editing, Funding Acquisition.

W. Vanduffel: Methodology, Writing – Review & Editing.

P.R. Roelfsema: Conceptualization, Resources, Supervision, Funding Acquisition, Writing – Review & Editing.

References

Ahmadi K, Fracasso A, Puzniak RJ, Gouws AD, Yakupov R, Speck O, Kaufmann J, Pestilli F, Dumoulin SO, Morland AB, Hoffmann MB. 2020. Triple visual hemifield maps in a case of optic chiasm hypoplasia. *NeuroImage* **215**:116822. doi:10/ggz9kc

Allman JM, Miezin F, McGuinness E. 1985. Stimulus specific responses from beyond the classical receptive field: neurophysiological mechanisms for local-global comparisons in visual neurons. *Annu Rev Neurosci* **8**:407–430. doi:10.1146/annurev.ne.08.030185.002203

Alvarez I, Smittenaar R, Handley SE, Liasis A, Sereno MI, Schwarzkopf DS, Clark CA. 2020. Altered visual population receptive fields in human albinism. *Cortex J Devoted Study Nerv Syst Behav* **128**:107–123. doi:10/ggz9km

Amano K, Wandell BA, Dumoulin SO. 2009. Visual Field Maps, Population Receptive Field Sizes, and Visual Field Coverage in the Human MT+ Complex. *J Neurophysiol* **102**:2704–2718. doi:10/d79g3p

Amiez C, Joseph JP, Procyk E. 2006. Reward Encoding in the Monkey Anterior Cingulate Cortex. *Cereb Cortex* **16**:1040–1055. doi:10/chz3d5

Arcaro MJ, Livingstone MS. 2017. Retinotopic Organization of Scene Areas in Macaque Inferior Temporal Cortex. *J Neurosci* **37**:7373–7389. doi:10.1523/JNEUROSCI.0569-17.2017

Arcaro MJ, Pinsk MA, Li X, Kastner S. 2011. Visuotopic Organization of Macaque Posterior Parietal Cortex: A Functional Magnetic Resonance Imaging Study. *J Neurosci* **31**:2064–2078. doi:10.1523/JNEUROSCI.3334-10.2011

Arsenault JT, Caspari N, Vandenberghe R, Vanduffel W. 2018. Attention Shifts Recruit the Monkey Default Mode Network. *J Neurosci* **38**:1202–1217. doi:10.1523/JNEUROSCI.1111-17.2017

Arthurs OJ, Boniface S. 2002. How well do we understand the neural origins of the fMRI BOLD signal? *Trends Neurosci* **25**:27–31. doi:10/cjsw99

Barlow H, Levick W, Westheimer G, Spinelli DN. 1966. Computer-plotted receptive fields. *Science* **154**:921.

Bartels A, Logothetis NK, Moutoussis K. 2008. fMRI and its interpretations: an illustration on directional selectivity in area V5/MT. *Trends Neurosci* **31**:444–453. doi:10.1016/j.tins.2008.06.004

Bartolo MJ, Gieselmann MA, Vuksanovic V, Hunter D, Sun L, Chen X, Delicato LS, Thiele A. 2011. Stimulus-induced dissociation of neuronal firing rates and local field potential gamma power and its relationship to the blood oxygen level-dependent signal in macaque primary visual cortex. *Eur J Neurosci* **34**:1857–1870. doi:10/b6cvvr

Beest EH van, Mukherjee S, Kirchberger L, Schnabel UH, Togt C van der, Teeuwen RRM, Barsegyan A, Meyer AF, Poort J, Roelfsema PR, Self MW. 2021. Mouse visual cortex contains a region of enhanced spatial resolution. *Nat Commun* **12**:4029. doi:10.1038/s41467-021-24311-5

Berens P, Keliris GA, Ecker AS, Logothetis NK, Tolias AS. 2008. Feature selectivity of the gamma-band of the local field potential in primate primary visual cortex. *Front Neurosci* **2**:199–207. doi:10.3389/neuro.01.037.2008

Best PB de, Raz N, Guy N, Ben-Hur T, Dumoulin SO, Pertzov Y, Levin N. 2019. Role of Population Receptive Field Size in Complex Visual Dysfunctions: A Posterior Cortical Atrophy Model. *JAMA Neurol* **76**:1391–1396. doi:10/ggz9kp

Binda P, Kurzawski JW, Lunghi C, Biagi L, Tosetti M, Morrone MC. 2018. Response to short-term deprivation of the human adult visual cortex measured with 7T BOLD. *eLife* **7**:e40014. doi:10/ggz9kw

Bokil H, Andrews P, Kulkarni JE, Mehta S, Mitra PP. 2010. Chronux: A platform for analyzing neural signals. *J Neurosci Methods* **192**:146–151. doi:10.1016/j.jneumeth.2010.06.020

Bonin V, Histed MH, Yurgenson S, Reid RC. 2011. Local diversity and fine-scale organization of receptive fields in mouse visual cortex. *J Neurosci Off J Soc Neurosci* **31**:18506–18521. doi:10/ffw6ss

Boynton GM. 2011. Spikes, BOLD, Attention, and Awareness: A comparison of electrophysiological and fMRI signals in V1. *J Vis* **11**:12–12. doi:10.1167/11.5.12

Brewer AA, Press WA, Logothetis NK, Wandell BA. 2002. Visual Areas in Macaque Cortex Measured Using Functional Magnetic Resonance Imaging. *J Neurosci* **22**:10416–10426. doi:10/gh2n5z

Britten KH, Heuer HW. 1999. Spatial summation in the receptive fields of MT neurons. *J Neurosci* **19**:5074–5084.

Burkhalter A, Van Essen D. 1986. Processing of color, form and disparity information in visual areas VP and V2 of ventral extrastriate cortex in the macaque monkey. *J Neurosci* **6**:2327–2351. doi:10/ghjkc9

Buzsaki G. 2006. Rhythms of the Brain. Oxford University Press.

Buzsaki G. 2004. Neuronal Oscillations in Cortical Networks. *Science* **304**:1926–1929. doi:10.1126/science.1099745

Buzsáki G. 2004. Large-scale recording of neuronal ensembles. *Nat Neurosci* **7**:446–451. doi:10.1038/nn1233

Cavanaugh P, Bair W, Movshon JA. 2002. Nature and interaction of signals from the receptive field center and surround in macaque V1 neurons. *J Neurophysiol* **88**:2530–2546.

Chen X, Possel JK, Wacongne C, van Ham AF, Klink PC, Roelfsema PR. 2017. 3D printing and modelling of customized implants and surgical guides for non-human primates. *J Neurosci Methods* **286**:38–55. doi:10.1016/j.jneumeth.2017.05.013

Chen X, Wang F, Fernandez E, Roelfsema PR. 2020. Shape perception via a high-channel-count neuroprosthesis in monkey visual cortex. *Science* **370**:1191–1196. doi:10/ghndcm

Cohen MR, Maunsell J. 2009. Attention improves performance primarily by reducing interneuronal correlations. *Nat Neurosci*. doi:10.1038/nn.2439

Cotton PL, Smith AT. 2007. Contralateral Visual Hemifield Representations in the Human Pulvinar Nucleus. *J Neurophysiol* **98**:1600–1609. doi:10/c2sx5j

Cox RW. 1996. AFNI: Software for Analysis and Visualization of Functional Magnetic Resonance Neuroimages. *Comput Biomed Res* **29**:162–173. doi:10/ctwqf6

Dekker TM, Schwarzkopf DS, de Haas B, Nardini M, Sereno MI. 2019. Population receptive field tuning properties of visual cortex during childhood. *Dev Cogn Neurosci* **37**:100614. doi:10/gg3qm4

DeSimone K, Viviano JD, Schneider KA. 2015. Population Receptive Field Estimation Reveals New Retinotopic Maps in Human Subcortex. *J Neurosci* **35**:9836–9847. doi:10.1523/JNEUROSCI.3840-14.2015

Drew PJ. 2019. Vascular and neural basis of the BOLD signal. *Curr Opin Neurobiol* **58**:61–69. doi:10/ggf3xg

Dubey A, Ray S. 2016. Spatial spread of local field potential is band-pass in the primary visual cortex. *J Neurophysiol* **116**:1986–1999. doi:10.1152/jn.00443.2016

Dumoulin SO, Knapen T. 2018. How Visual Cortical Organization Is Altered by Ophthalmologic and Neurologic Disorders. *Annu Rev Vis Sci* **4**:357–379. doi:10/ggt2mw

Dumoulin SO, Wandell BA. 2008. Population receptive field estimates in human visual cortex. *NeuroImage* **39**:647–660. doi:10.1016/j.neuroimage.2007.09.034

Einevoll GT, Kayser C, Logothetis NK, Panzeri S. 2013. Modelling and analysis of local field potentials for studying the function of cortical circuits. *Nat Rev Neurosci* **14**:770–785. doi:10/f5drx4

Ekman M, Roelfsema PR, Lange FP de. 2020. Object selection by automatic spreading of top-down attentional signals in V1. *J Neurosci* JN-RM-0438-20. doi:10.1523/jneurosci.0438-20.2020

Ekstrom A. 2010. How and when the fMRI BOLD signal relates to underlying neural activity: The danger in dissociation. *Brain Res Rev* **62**:233–244. doi:10/cm4cxg

Ekstrom LB, Roelfsema PR, Arsenault JT, Bonmassar G, Vanduffel W. 2008. Bottom-Up Dependent Gating of Frontal Signals in Early Visual Cortex. *Science* **321**:414–417. doi:10.1126/science.1153276

Engel SA. 2012. The development and use of phase-encoded functional MRI designs. *NeuroImage* **62**:1195–1200. doi:10.1016/j.neuroimage.2011.09.059

Engel SA, Rumelhart DE, Wandell BA, Lee AT, Glover GH, Chichilnisky E-J, Shadlen MN. 1994. fMRI of human visual cortex. *Nature* **369**:525–525. doi:10/dhzvzr

Erwin E, Baker FH, Busen WF, Malpeli JG. 1999. Relationship between laminar topology and retinotopy in the rhesus lateral geniculate nucleus: Results from a functional atlas. *J Comp Neurol* **407**:92–102. doi:10.1002/(SICI)1096-9861(19990428)407:1<92::AID-CNE7>3.0.CO;2-1

Farivar R, Vanduffel W. 2014. Functional MRI of Awake Behaving Macaques Using Standard EquipmentAdvanced Brain Neuroimaging Topics in Health and Disease - Methods and Applications.

Felleman DJ, Van Essen DC. 1987. Receptive field properties of neurons in area V3 of macaque monkey extrastriate cortex. *J Neurophysiol* **57**:889–920. doi:10/gg3c6t

Fischl B. 2012. FreeSurfer. *NeuroImage* **62**:774–781. doi:10/fzcbq3

Fouragnan EF, Chau BKH, Folloni D, Kolling N, Verhagen L, gge MK-F x000FC, Tankelevitch L, Papageorgiou GK, Aubry J-F, Sallet J, Rushworth MFS. 2019. The macaque anterior cingulate cortex translates counterfactual choice value into actual behavioral change. *Nat Neurosci* 1–19. doi:10.1038/s41593-019-0375-6

Fox AS, Holley D, Klink PC, Arbuckle SA, Barnes CA, Diedrichsen J, Kwok SC, Kyle C, Pruszynski JA, Seidlitz J, Zhou X, Poldrack RA, Gorgolewski KJ. 2021. Sharing voxelwise neuroimaging results from rhesus monkeys and other species with Neurovault. *NeuroImage* **225**:117518. doi:10/gh2n52

Gao JS, Huth AG, Lescroart MD, Gallant JL. 2015. Pycortex: an interactive surface visualizer for fMRI. *Front Neuroinformatics* **9**:162–12. doi:10.3389/fninf.2015.00023

Gattass R, Gross CG, Sandell JH. 1981. Visual topography of V2 in the macaque. *J Comp Neurol* **201**:519–539. doi:10/b3zkrv

Gattass R, Nascimento-Silva S, Soares JGM, Lima B, Jansen AK, Diogo ACM, Farias MF, Botelho MMEP, Mariani OS, Azzi JCB, Fiorani M. 2005. Cortical visual areas in monkeys: location, topography, connections, columns, plasticity and cortical dynamics. *Philos Trans R Soc Lond B Biol Sci* **360**:709–731. doi:10.1098/rstb.2005.1629

Gattass R, Sousa AP, Gross CG. 1988. Visuotopic organization and extent of V3 and V4 of the macaque. *J Neurosci Off J Soc Neurosci* **8**:1831–1845.

Gattass R, Sousa AP, Rosa MG. 1987. Visual topography of V1 in the Cebus monkey. *J Comp Neurol* **259**:529–548. doi:10/c7h4mp

Goense JBM, Logothetis NK. 2008. Neurophysiology of the BOLD fMRI signal in awake monkeys. *Curr Biol* **18**:631–640. doi:10.1016/j.cub.2008.03.054

Gorgolewski KJ, Varoquaux G, Rivera G, Schwarz Y, Ghosh SS, Maumet C, Sochat VV, Nichols TE, Poldrack RA, Poline J-B, Yarkoni T, Margulies DS. 2015. NeuroVault.org: a web-based repository for collecting and sharing unthresholded statistical maps of the human brain. *Front Neuroinformatics* **9**. doi:10/ggz9kx

Green T, Hosseini H, Piccirilli A, Ishak A, Grill-Spector K, Reiss AL. 2019. X-Chromosome Insufficiency Alters Receptive Fields across the Human Early Visual Cortex. *J Neurosci Off J Soc Neurosci* **39**:8079–8088. doi:10/ggz9ks

Greene CA, Dumoulin SO, Harvey BM, Ress D. 2014. Measurement of population receptive fields in human early visual cortex using back-projection tomography. *J Vis* **14**:17–17. doi:10.1167/14.1.17

Griffis JC, Elkhetali AS, Burge WK, Chen RH, Bowman AD, Szaflarski JP, Visscher KM. 2017. Retinotopic patterns of functional connectivity between V1 and large-scale brain networks during resting fixation. *NeuroImage* **146**:1071–1083. doi:10/f9vmmf

Griffiths BJ, Mayhew SD, Mullinger KJ, Jorge J, Charest I, Wimber M, Hanslmayr S. 2019. Alpha/beta power decreases track the fidelity of stimulus-specific information. *eLife* **8**:e49562. doi:10/ggd4tv

Haak KV, Winawer J, Ben M Harvey, Renken R, Dumoulin SO, Wandell BA, Cornelissen FW. 2013. Connective field modeling. *NeuroImage* **66**:376–384. doi:10.1016/j.neuroimage.2012.10.037

Hartline HK. 1938. The response of single optic nerve fibers of the vertebrate eye to illumination of the retina. *Am J Physiol-Leg Content*. doi:10/ggt2mv

Harvey BM, Dumoulin SO, Fracasso A, Paul JM. 2020. A Network of Topographic Maps in Human Association Cortex Hierarchically Transforms Visual Timing-Selective Responses. *Curr Biol* **30**:1424-1434.e6. doi:10/ggt2mz

Harvey BM, Fracasso A, Petridou N, Dumoulin SO. 2015. Topographic representations of object size and relationships with numerosity reveal generalized quantity processing in human parietal cortex. *Proc Natl Acad Sci* 201515414–6. doi:10.1073/pnas.1515414112

Harvey BM, Vansteensel MJ, Ferrier CH, Petridou N, Zuiderbaan W, Aarnoutse EJ, Bleichner MG, Dijkerman HC, van Zandvoort MJE, Leijten FSS, Ramsey NF, Dumoulin SO. 2013. Frequency specific spatial interactions in human electrocorticography: V1 alpha oscillations reflect surround suppression. *NeuroImage* **65**:424–432. doi:10.1016/j.neuroimage.2012.10.020

He D, Wang Y, Fang F. 2019. The Critical Role of V2 Population Receptive Fields in Visual Orientation Crowding. *Curr Biol* **29**:2229-2236.e3. doi:10/ggz9kt

Hubel DH, Wiesel TN. 1998. Early exploration of the visual cortex. *Neuron* **20**:401–412.

Hubel DH, Wiesel TN. 1974. Uniformity of monkey striate cortex: a parallel relationship between field size, scatter, and magnification factor. *J Comp Neurol* **158**:295–305. doi:10/d4tnkt

Hubel DH, Wiesel TN. 1968. Receptive fields and functional architecture of monkey striate cortex. *J Physiol* **195**:215–243.

Hubel DH, Wiesel TN. 1962. Receptive fields, binocular interaction and functional architecture in the cat's visual cortex. *J Physiol* **160**:106–154.

Hubel DH, Wiesel TN. 1959. Receptive fields of single neurones in the cat's striate cortex. *J Physiol* **148**:574–591.

Hughes AE, Greenwood JA, Finlayson NJ, Schwarzkopf DS. 2019. Population receptive field estimates for motion-defined stimuli. *NeuroImage* **199**:245–260. doi:10/ggz9kv

Janssens T, Zhu Q, Popivanov ID, Vanduffel W. 2014. Probabilistic and Single-Subject Retinotopic Maps Reveal the Topographic Organization of Face Patches in the Macaque Cortex. *J Neurosci* **34**:10156–10167. doi:10.1523/JNEUROSCI.2914-13.2013

Jenkinson M, Bannister P, Brady M, Smith S. 2002. Improved Optimization for the Robust and Accurate Linear Registration and Motion Correction of Brain Images. *NeuroImage* **17**:825–841. doi:10/ctfvqv

Kajikawa Y, Schroeder CE. 2011. How Local Is the Local Field Potential? *Neuron* **72**:847–858. doi:10.1016/j.neuron.2011.09.029

Katzner S, Nauhaus I, Benucci A, Bonin V, Ringach DL, Carandini M. 2009. Local origin of field potentials in visual cortex. *Neuron* **61**:35–41. doi:10.1016/j.neuron.2008.11.016

Kay KN, Winawer J, Mezer A, Wandell BA. 2013. Compressive spatial summation in human visual cortex. *J Neurophysiol* **110**:481–494. doi:10.1152/jn.00105.2013

Keliris GA, Li Q, Papanikolaou A, Logothetis NK, Smirnakis SM. 2019. Estimating average single-neuron visual receptive field sizes by fMRI. *Proc Natl Acad Sci U S A* **62**:201809612–10. doi:10.1073/pnas.1809612116

Klink PC, Dagnino B, Gariel-Mathis M-A, Roelfsema PR. 2017. Distinct Feedforward and Feedback Effects of Microstimulation in Visual Cortex Reveal Neural Mechanisms of Texture Segregation. *Neuron* 1–16. doi:10.1016/j.neuron.2017.05.033

Knierim JJ, van Essen DC. 1992. Neuronal responses to static texture patterns in area V1 of the alert macaque monkey. *J Neurophysiol* **67**:961–980. doi:10/gg3qpb

Kolster H, Janssens T, Orban GA, Vanduffel W. 2014. The Retinotopic Organization of Macaque Occipitotemporal Cortex Anterior to V4 and Caudoventral to the Middle Temporal (MT) Cluster. *J Neurosci* **34**:10168–10191. doi:10.1523/JNEUROSCI.3288-13.2014

Kolster H, Mandeville JB, Arsenault JT, Ekstrom LB, Wald LL, Vanduffel W. 2009. Visual field map clusters in macaque extrastriate visual cortex. *J Neurosci* **29**:7031–7039. doi:10.1523/JNEUROSCI.0518-09.2009

Kolster H, Peeters R, Orban GA. 2010. The retinotopic organization of the human middle temporal area MT/V5 and its cortical neighbors. *J Neurosci* **30**:9801–9820. doi:10.1523/JNEUROSCI.2069-10.2010

Kreiman G, Hung CP, Kraskov A, Quian Quiroga R, Poggio T, DiCarlo JJ. 2006. Object selectivity of local field potentials and spikes in the macaque inferior temporal cortex. *Neuron* **49**:433–445. doi:10.1016/j.neuron.2005.12.019

Larsson J, Heeger DJ. 2006. Two retinotopic visual areas in human lateral occipital cortex. *J Neurosci* **26**:13128–13142. doi:10.1523/JNEUROSCI.1657-06.2006

Lerma-Usabiaga G, Winawer J, Wandell BA. 2021. Population Receptive Field Shapes in Early Visual Cortex Are Nearly Circular. *J Neurosci* **41**:2420–2427. doi:10.1523/JNEUROSCI.3052-20.2021

Łęski S, Lindén H, Tetzlaff T, Pettersen KH, Einevoll GT. 2013. Frequency Dependence of Signal Power and Spatial Reach of the Local Field Potential. *PLOS Comput Biol* **9**:e1003137. doi:10/f237jb

Li X, Morgan PS, Ashburner J, Smith J, Rorden C. 2016. The first step for neuroimaging data analysis: DICOM to NIfTI conversion. *J Neurosci Methods* **264**:47–56. doi:10.1016/j.jneumeth.2016.03.001

Lima B, Cardoso MMB, Sirotin YB, Das A. 2014. Stimulus-Related Neuroimaging in Task-Engaged Subjects Is Best Predicted by Concurrent Spiking. *J Neurosci* **34**:13878–13891. doi:10.1523/JNEUROSCI.1595-14.2014

Logothetis NK. 2010. Neurovascular uncoupling: Much ado about nothing. *Front Neuroenergetics* **2**. doi:10.3389/fnene.2010.00002

Logothetis NK. 2003. The underpinnings of the BOLD functional magnetic resonance imaging signal. *J Neurosci* **23**:3963–3971.

Logothetis NK, Pauls J, Augath MA, Trinath T, Oeltermann A. 2001. Neurophysiological investigation of the basis of the fMRI signal. *Nature* **412**:150–157.

Logothetis NK, Wandell BA. 2004. Interpreting the BOLD Signal. *Annu Rev Physiol* **66**:735–769. doi:10.1146/annurev.physiol.66.082602.092845

Maier A, Wilke M, Aura CJ, Zhu C, Ye FQ, Leopold DA. 2008. Divergence of fMRI and neural signals in V1 during perceptual suppression in the awake monkey. *Nat Neurosci* **11**:1193–1200. doi:10.1038/nn.2173

Mantini D, Gerits A, Nelissen K, Durand J-B, Joly O, Simone L, Sawamura H, Wardak C, Orban GA, Buckner RL, Vanduffel W. 2011. Default mode of brain function in monkeys. *J Neurosci* **31**:12954–12962. doi:10.1523/JNEUROSCI.2318-11.2011

Merkel C, Hopf J-M, Schoenfeld MA. 2018. Spatial elongation of population receptive field profiles revealed by model-free fMRI back-projection. *Hum Brain Mapp* **39**:2472–2481. doi:10.1002/hbm.24015

Messinger A, Sirmpilatze N, Heuer K, Loh KK, Mars RB, Sein J, Xu T, Glen D, Jung B, Seidlitz J, Taylor P, Toro R, Garza-Villarreal EA, Sponheim C, Wang X, Benn RA, Cagna B, Dadarwal R, Evrard HC, Garcia-Saldivar P, Giavasis S, Hartig R, Lepage C, Liu C, Majka P, Merchant H, Milham MP, Rosa MGP, Tasserie J, Uhrig L, Margulies DS, Klink PC. 2021. A collaborative resource platform for non-human primate neuroimaging. *NeuroImage* **226**:117519. doi:10/ghkvj8

Mo C, He D, Fang F. 2017. Attention priority map of face images in human early visual cortex. *J Neurosci* 1206–17. doi:10.1523/JNEUROSCI.1206-17.2017

Mukamel R, Gelbard H, Arieli A, Hasson U, Fried I, Malach R. 2005. Coupling between neuronal firing, field potentials, and FMRI in human auditory cortex. *Science* **309**:951–954. doi:10.1126/science.1110913

Nelson MJ, Pouget P. 2010. Do Electrode Properties Create a Problem in Interpreting Local Field Potential Recordings? *J Neurophysiol* **103**:2315–2317. doi:10.1152/jn.00157.2010

Newsome WT, Maunsell JH, Van Essen DC. 1986. Ventral posterior visual area of the macaque: visual topography and areal boundaries. *J Comp Neurol* **252**:139–153. doi:10/bvpwvw

Niessing J, Ebisch B, Schmidt KE, Niessing M, Singer W, Galuske RAW. 2005. Hemodynamic Signals Correlate Tightly with Synchronized Gamma Oscillations. *Science* **309**:948–951. doi:10/bz27m7

Nir Y, Fisch L, Mukamel R, Gelbard-Sagiv H, Arieli A, Fried I, Malach R. 2007. Coupling between Neuronal Firing Rate, Gamma LFP, and BOLD fMRI Is Related to Interneuronal Correlations. *Curr Biol* **17**:1275–1285. doi:10/b93t7b

Oleksiak A, Klink PC, Postma A, van der Ham IJM, Lankheet MJ, van Wezel RJA. 2011. Spatial summation in macaque parietal area 7a follows a winner-take-all rule. *J Neurophysiol* **105**:1150–1158. doi:10.1152/jn.00907.2010

Palmer C, Cheng S, Seidemann E. 2007. Linking neuronal and behavioral performance in a reaction-time visual detection task. *J Neurosci* **27**:8122–8137.

Patel GH, Shulman GL, Baker JT, Akbudak E, Snyder AZ, Snyder LH, Corbetta M. 2010. Topographic organization of macaque area LIP. *Proc Natl Acad Sci* **107**:4728–4733. doi:10/c9cfrp

Poltoratski S, Maier A, Newton AT, Tong F. 2019. Figure-Ground Modulation in the Human Lateral Geniculate Nucleus Is Distinguishable from Top- Down Attention. *Curr Biol* 1–11. doi:10.1016/j.cub.2019.04.068

Poltoratski S, Tong F. 2020. Resolving the spatial profile of figure enhancement in human V1 through population receptive field modeling. *J Neurosci* JN-RM-2377-19. doi:10/gg3qnq

Poort J, Raudies F, Wannig A, Lamme VAF, Neumann H, Roelfsema PR. 2012. The role of attention in figure-ground segregation in areas v1 and v4 of the visual cortex. *Neuron* **75**:143–156. doi:10.1016/j.neuron.2012.04.032

Priebe NJ. 2008. The relationship between subthreshold and suprathreshold ocular dominance in cat primary visual cortex. *J Neurosci* **28**:8553–8559. doi:10.1523/JNEUROSCI.2182-08.2008

Puckett AM, Bollmann S, Junday K, Barth M, Cunnington R. 2020. Bayesian population receptive field modeling in human somatosensory cortex. *NeuroImage* **208**:116465. doi:10/ggt2mx

Rees G, Friston K, Koch C. 2000. A direct quantitative relationship between the functional properties of human and macaque V5. *Nat Neurosci* **3**:716–723.

Reveley C, Gruslys A, Ye F, Glen D, Samaha J, Russ B, Saad Z, Seth A, Leopold D, Saleem K. 2017. Three-Dimensional Digital Template Atlas of the Macaque Brain. *Cereb Cortex* **27**:4463–4477. doi:10/ggr64q

Rima S, Cottereau BR, Héjja-Brichard Y, Trotter Y, Durand J-B. 2020. Wide-field retinotopy reveals a new visuotopic cluster in macaque posterior parietal cortex. *Brain Struct Funct* **225**:2447–2461. doi:10/ghjdhs

Rosa MG. P, Piñon MC, Gattass R, Sousa APB. 2000. Third tier ventral extrastriate cortex in the New World monkey, Cebus apella. *Exp Brain Res* **132**:287–305. doi:10/bjf9dn

Rosa MGP, Sousa APB, Gattass R. 1988. Representation of the visual field in the second visual area in the Cebus monkey. *J Comp Neurol* **275**:326–345. doi:10/bjwfm5

Rousche PJ, Normann RA. 1998. Chronic recording capability of the Utah Intracortical Electrode Array in cat sensory cortex. *J Neurosci Methods* **82**:1–15. doi:10/cpcdzd

Saygin AP, Sereno MI. 2008. Retinotopy and Attention in Human Occipital, Temporal, Parietal, and Frontal Cortex. *Cereb Cortex* **18**:2158–2168. doi:10/dtms3d

Schneider KA, Richter MC, Kastner S. 2004. Retinotopic Organization and Functional Subdivisions of the Human Lateral Geniculate Nucleus: A High-Resolution Functional Magnetic Resonance Imaging Study. *J Neurosci* **24**:8975–8985. doi:10/bvzk25

Scholvinck ML, Maier A, Frank QY, Duyn JH, Leopold DA. 2010. Neural basis of global resting-state fMRI activity. *Proc Natl Acad Sci* **107**:10238–10243. doi:10.1073/pnas.0913110107/-/DCSupplemental

Schwarzkopf DS, Anderson EJ, Haas B de, White SJ, Rees G. 2014. Larger Extrastriate Population Receptive Fields in Autism Spectrum Disorders. *J Neurosci* **34**:2713–2724. doi:10/f5sx87

Seidlitz J, Sponheim C, Glen D, Ye FQ, Saleem KS, Leopold DA, Ungerleider L, Messinger A. 2018. A population MRI brain template and analysis tools for the macaque. *NeuroImage* **170**:121–131. doi:10/gc6vs3

Sereno MI, Dale AM, Reppas JB, Kwong KK, Belliveau JW, Brady TJ, Rosen BR, Tootell RB. 1995. Borders of multiple visual areas in humans revealed by functional magnetic resonance imaging. *Science* **268**:889–893.

Shao Y, Keliris GA, Papanikolaou A, Fischer MD, Zobor D, Jägle H, Logothetis NK, Smirnakis SM. 2013. Visual cortex organisation in a macaque monkey with macular degeneration. *Eur J Neurosci* **38**:3456–3464. doi:10.1111/ejn.12349

Shen L, Han B, Lange FP de. 2020. Apparent motion induces activity suppression in early visual cortex and impairs visual detection. *J Neurosci*. doi:10/ggz9kf

Sherrington CS. 1906. Observations on the scratch-reflex in the spinal dog. *J Physiol* **34**:1–50. doi:10/ggj5gs

Shmuel A, Augath M, Oeltermann A, Logothetis NK. 2006. Negative functional MRI response correlates with decreases in neuronal activity in monkey visual area V1. *Nat Neurosci* **9**:569–577. doi:10/d3xwp9

Siegel M, Donner TH, Oostenveld R, Fries P, Engel AK. 2008. Neuronal synchronization along the dorsal visual pathway reflects the focus of spatial attention. *Neuron* **60**:709–719. doi:10.1016/j.neuron.2008.09.010

Silson EH, Reynolds RC, Kravitz DJ, Baker CI. 2018. Differential Sampling of Visual Space in Ventral and Dorsal Early Visual Cortex. *J Neurosci* **38**:2294–2303. doi:10.1523/JNEUROSCI.2717-17.2018

Sirotin YB, Das A. 2009. Anticipatory haemodynamic signals in sensory cortex not predicted by local neuronal activity. *Nature* **457**:475–479. doi:10/fcmb52

Smith AT, Williams AL, Singh KD. 2004. Negative BOLD in the visual cortex: Evidence against blood stealing. *Hum Brain Mapp* **21**:213–220. doi:10/chhjsd

Stoll S, Finlayson NJ, Schwarzkopf DS. 2020. Topographic Signatures of Global Object Perception in Human Visual Cortexa. *NeuroImage* 116926. doi:10/ggz9kg

Supèr H, Roelfsema PR. 2005. Chronic multiunit recordings in behaving animals: advantages and limitations. *Prog Brain Res* **147**:263–282. doi:10/cgb67n

Szinte M, Knapen T. 2019. Visual Organization of the Default Network. *Cereb Cortex*. doi:10/ggtm5t

Tani N, Joly O, Iwamuro H, Uhrig L, Wiggins CJ, Poupon C, Kolster H, Vanduffel W, Le Bihan D, Palfi S, Jarraya B. 2011. Direct visualization of non-human primate subcortical nuclei with contrast-enhanced high field MRI. *NeuroImage* **58**:60–68. doi:10.1016/j.neuroimage.2011.06.019

Thomas JM, Huber E, Stecker GC, Boynton GM, Saenz M, Fine I. 2015. Population receptive field estimates of human auditory cortex. *NeuroImage* **105**:428–439. doi:10/f6sbd8

van Es DM, van der Zwaag W, Knapen T. 2019. Topographic Maps of Visual Space in the Human Cerebellum. *Curr Biol* 1–10. doi:10.1016/j.cub.2019.04.012

Van Essen DC, Newsome WT, Maunsell JHR. 1984. The visual field representation in striate cortex of the macaque monkey: Asymmetries, anisotropies, and individual variability. *Vision Res* **24**:429–448. doi:10/crf3q8

van Kerkoerle T, Self MW, Dagnino B, Gariel-Mathis M-A, Poort J, van der Togt C, Roelfsema PR. 2014. Alpha and gamma oscillations characterize feedback and feedforward processing in monkey visual cortex. *Proc Natl Acad Sci U S A* **111**:14332–14341. doi:10.1073/pnas.1402773111

Vanduffel W, Fize D, Mandeville JB, Nelissen K, Van Hecke P, Rosen BR, Tootell RB, Orban GA. 2001. Visual motion processing investigated using contrast agent-enhanced fMRI in awake behaving monkeys. *Neuron* **32**:565–577.

Victor JD, Purpura K, Katz E, Mao B. 1994. Population encoding of spatial frequency, orientation, and color in macaque V1. *J Neurophysiol* **72**:2151–2166. doi:10.1152/jn.1994.72.5.2151

Viswam V, Obien MEJ, Franke F, Frey U, Hierlemann A. 2019. Optimal Electrode Size for Multi-Scale Extracellular-Potential Recording From Neuronal Assemblies. *Front Neurosci* **13**:385. doi:10.3389/fnins.2019.00385

Viswanathan A, Freeman RD. 2007. Neurometabolic coupling in cerebral cortex reflects synaptic more than spiking activity. *Nat Neurosci* **10**:1308–1312. doi:10/cbxvpj

Wandell BA, Dumoulin SO, Brewer AA. 2007. Visual field maps in human cortex. *Neuron* **56**:366–383. doi:10.1016/j.neuron.2007.10.012

Wandell BA, Winawer J. 2015. Computational neuroimaging and population receptive fields. *Trends Cogn Sci* **19**:349–357. doi:10.1016/j.tics.2015.03.009

Wandell BA, Winawer J. 2010. Imaging retinotopic maps in the human brain. *Vision Res*. doi:10.1016/j.visres.2010.08.004

Ward MP, Rajdev P, Ellison C, Irazoqui PP. 2009. Toward a comparison of microelectrodes for acute and chronic recordings. *Brain Res* **1282**:183–200. doi:10.1016/j.brainres.2009.05.052

Welbourne LE, Morland AB, Wade AR. 2018. Population receptive field (pRF) measurements of chromatic responses in human visual cortex using fMRI. *NeuroImage* **167**:84–94. doi:10.1016/j.neuroimage.2017.11.022

Winawer J, Kay KN, Foster BL, Rauschecker AM, Parvizi J, Wandell BA. 2013. Asynchronous Broadband Signals Are the Principal Source of the BOLD Response in Human Visual Cortex. *Curr Biol* **23**:1145–1153. doi:10.1016/j.cub.2013.05.001

Winder AT, Echagarruga C, Zhang Q, Drew PJ. 2017. Weak correlations between hemodynamic signals and ongoing neural activity during the resting state. *Nat Neurosci* 1–16. doi:10.1038/s41593-017-0007-y

Womelsdorf T, Fries P. 2007. The role of neuronal synchronization in selective attention. *Curr Opin Neurobiol* **17**:154–160. doi:10.1016/j.conb.2007.02.002

Woolrich MW, Behrens TEJ, Smith SM. 2004. Constrained linear basis sets for HRF modelling using Variational Bayes. *NeuroImage* **21**:1748–1761. doi:10.1016/j.neuroimage.2003.12.024

Worden MS, Foxe JJ, Wang N, Simpson GV. 2000. Anticipatory biasing of visuospatial attention indexed by retinotopically specific alpha-band electroencephalography increases over occipital cortex. *J Neurosci Off J Soc Neurosci* **20**:RC63.

Xing D, Yeh C-I, Shapley RM. 2009. Spatial spread of the local field potential and its laminar variation in visual cortex. *J Neurosci* **29**:11540–11549. doi:10.1523/JNEUROSCI.2573-09.2009

Yoshor D, Bosking WH, Ghose GM, Maunsell JHR. 2007. Receptive Fields in Human Visual Cortex Mapped with Surface Electrodes. *Cereb Cortex* **17**:2293–2302. doi:10/ctb723

Zeidman P, Silson EH, Schwarzkopf DS, Baker CI, Penny W. 2018. Bayesian population receptive field modelling. *NeuroImage*, New advances in encoding and decoding of brain signals **180**:173–187. doi:10.1016/j.neuroimage.2017.09.008

Zhu Q, Vanduffel W. 2019. Submillimeter fMRI reveals a layout of dorsal visual cortex in macaques, remarkably similar to New World monkeys. *Proc Natl Acad Sci* **32**:201805561–6. doi:10.1073/pnas.1805561116

Zuiderbaan W, Harvey BM, Dumoulin SO. 2017. Image identification from brain activity using the population receptive field model. *PLOS ONE* **12**:e0183295. doi:10/gfwjvr

Zuiderbaan W, Harvey BM, Dumoulin SO. 2012. Modeling center-surround configurations in population receptive fields using fMRI. *J Vis* **12**:10–10. doi:10.1167/12.3.10

761

762 # Supplemental Information

763

764 - **Supplemental Table 1**
765 - ROI abbreviations
766 - **Supplemental Figure 1-12**
767 - Supplemental Figure 1: related to Figure 2C
768 - Supplemental Figure 2: related to Figure 3
769 - Supplemental Figure 3: related to Figure 4
770 - Supplemental Figure 4: related to Figure 4
771 - Supplemental Figure 5A: related to Figure 5A,B
772 - Supplemental Figure 5B: related to Figure 5C,D
773 - Supplemental Figure 6: related to Figure 6
774 - Supplemental Figure 7: related to Figure 8
775 - Supplemental Figure 8: related to Figure 8
776 - Supplemental Figure 9: related to Figure 8
777 - Supplemental Figure 10: related to Figure 10
778 - Supplemental Figure 11: related to Figure 10
779 - Supplemental Figure 12: related to Figure 12
780 - Supplemental Figure 13: related to Materials and Methods

781 ## Supplemental Table 1: ROI abbreviations

782

ROI abbreviation	ROI full name (BA = Brodmann Area)
V1	Primary visual cortex
V2	Visual area V2
V3	Visual area V3
V3A	Visual area V3A
V4	Visual area V4
MT	Middle Temporal visual area
MST	Medial Superior Temporal cortex
TEO	Inferior temporal cortical area TEO
TAa	Temporal area TAa
Tpt	Auditory association cortex (Temporoparietal)
TPO	Temporo-parietal-occipital junction
FST	Fundus of the superior temporal visual areas
A1	Primary auditory cortex
ML	Middle lateral, belt region of the auditory cortex
AL	Anterior lateral, belt region of the auditory cortex
PULV	Pulvinar
LGN	Lateral geniculate nucleus
STR	Striatum
LIP	Lateral intraparietal cortex
VIP	Ventral intraparietal cortex
5	BA 5 (parietal area PE)
7	BA 7, includes BA 7a (Opt/PG) and BA 7b (PFG/PF)
SI	Primary somatosensory cortex (BA 1, 2, and 3)
SII	Secondary somatosensory cortex
F2	Area F2, dorsal caudal premotor cortex
F4	Area F4, ventral caudal premotor cortex
F5	Area F5, ventral rostral premotor cortex
F7	Area F7, dorsal rostral premotor cortex
8	BA 8 (includes the Frontal Eye Fields)
CINp	Poster cingulate cortex (BA 23)
CINa	Anterior cingulate cortex (BA 24c, and BA 32)
OFC	Orbitofrontal cortex (BA 12)
INS	Insular cortex (includes BA 13)
DLPFC	Dorsolateral prefrontal cortex (BA 10, and BA 46)
VMPFC	Ventromedial prefrontal cortex (BA 14)

783

Occipital lobe	Temporal lobe	Subcortical	Parietal lobe	Frontal lobe

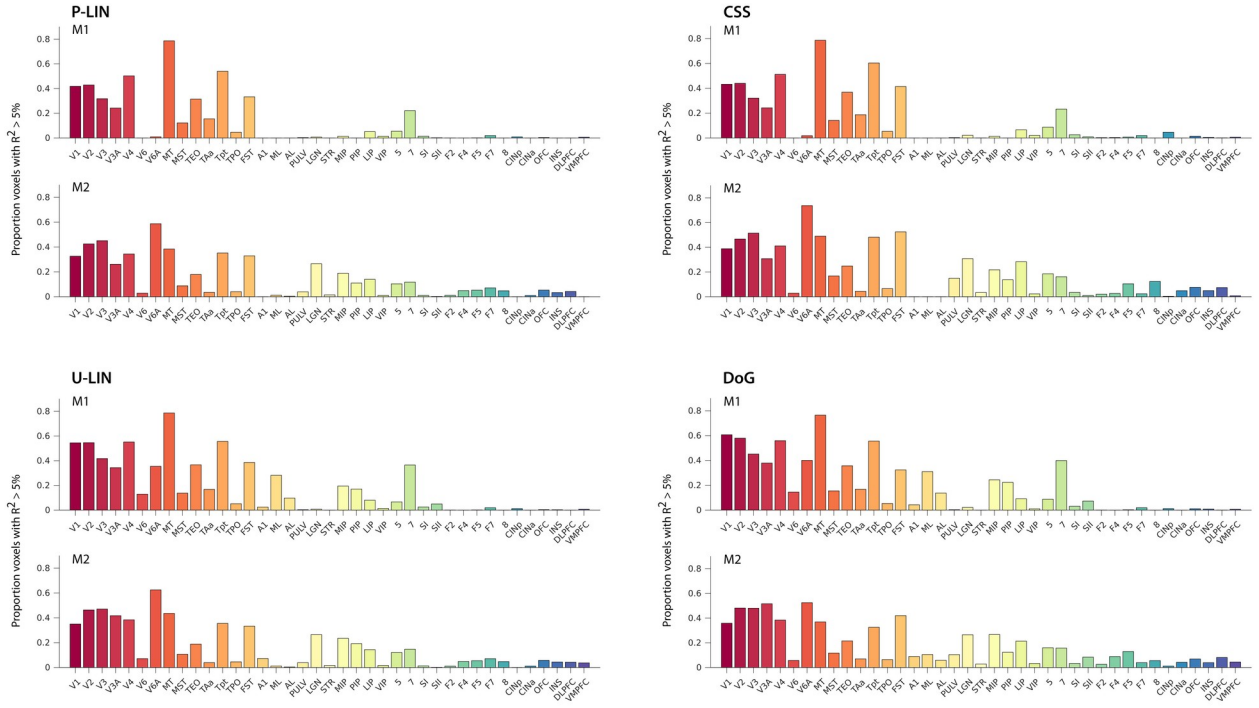

Supplemental Figure 1. Proportion of voxels with R^2 > 5% per ROI. For both animals (M1, M2) and all four pRF models. Supplement to Figure 2C that reports absolute numbers of voxels per area.

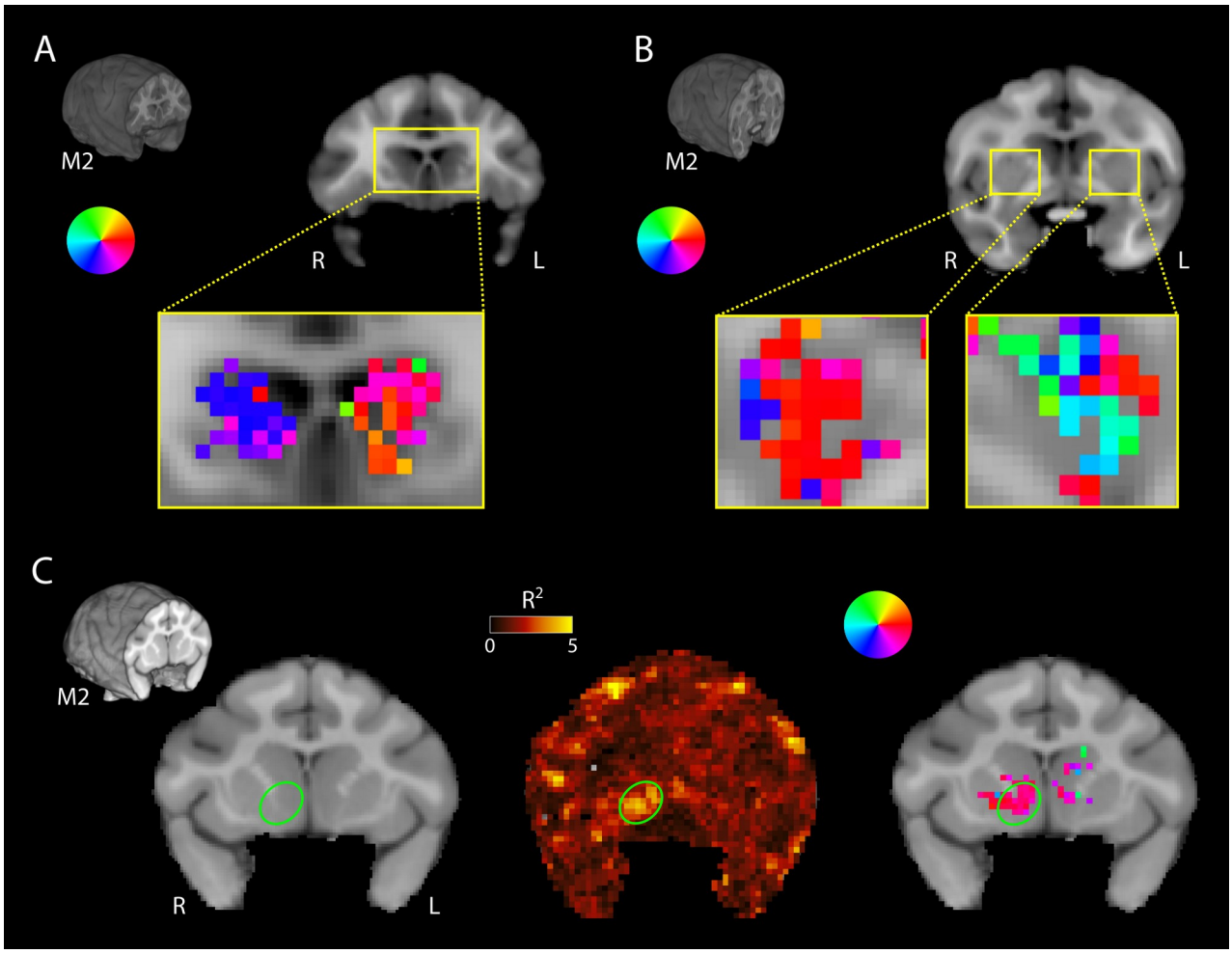

Supplemental Figure 2. Striatal pRFs. (A) In M2, the head of the caudate nucleus in the striatum contained retinotopic maps of the lower contralateral visual field. Neurons in the head of the caudate have long been known to play a role in processing visual information in a reward-related context (Hikosaka et al., 1989a, 1989b; Rolls et al., 1983). **(B)** In the more posterior striatum of M2, retinotopic information was also present. While spatial preferences were more mixed here, there was a dominant representation of the ipsilateral visual field. **(C)** Voxels in the right nucleus accumbens (Nac) have ipsilateral pRFs. The right NAc in the ventral striatum (green outline) is retinotopically tuned in both monkeys (only M2 shown). Although R^2 values are lower than in the cortex or thalamus, they stand out from the surrounding regions. Polar angle maps of the fitted pRFs indicate that the right NAc is tuned to visual information in the right (ipsilateral) visual field.

786

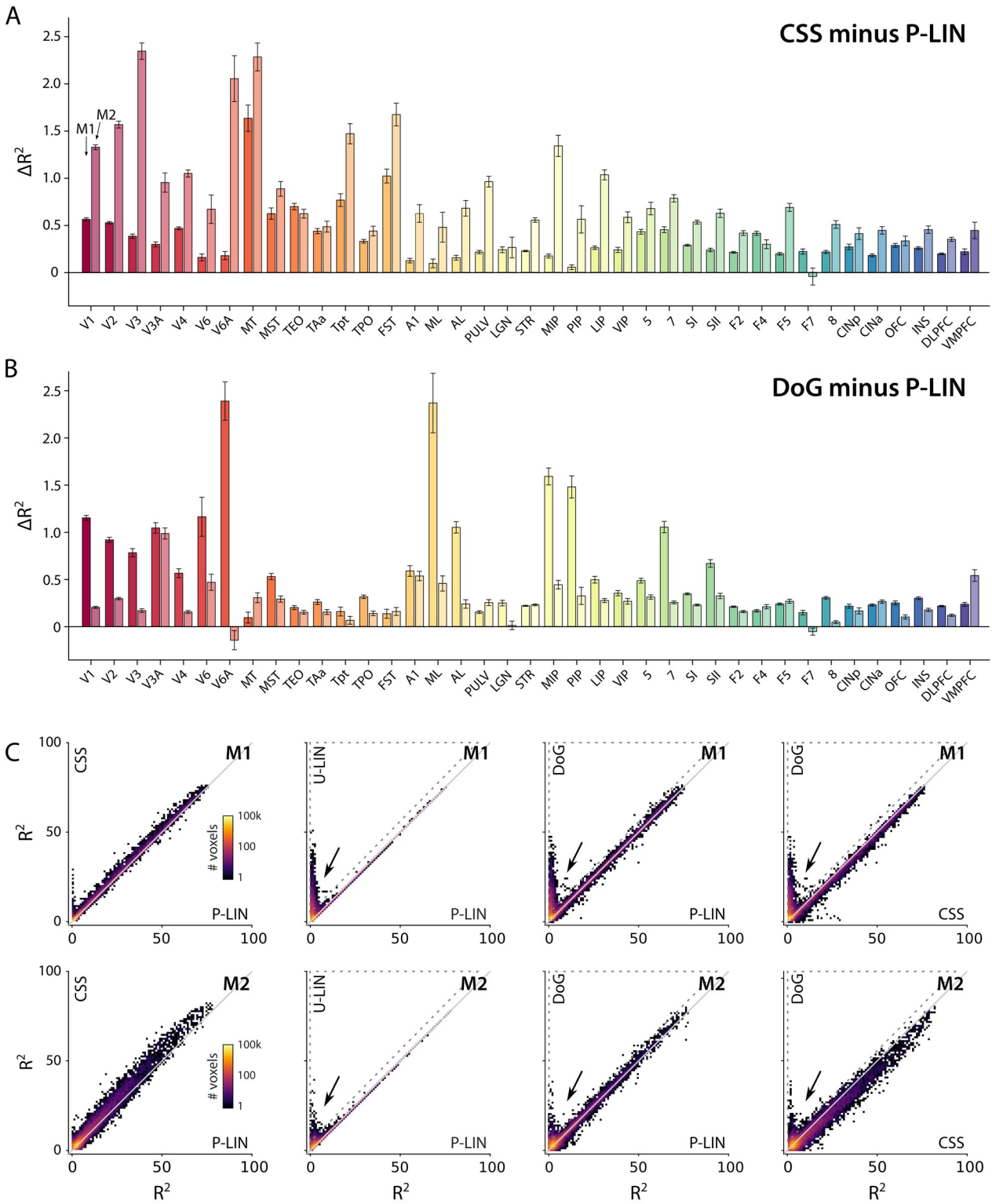

Supplemental Figure 3. (A-B) Fit accuracy advantage of CSS and DoG models across brain areas. Both the CSS (**A**) and DoG (**B**) models had better fits (cross-validated R2) than the P-LIN model across virtually all brain regions with retinotopic information in both monkeys. **(C)** Comparison of R^2 across pRF models for both monkeys. Data is in R^2 bins of 1% × 1%. Colors represent number of voxels per bin. The CSS model fits best across the board. The U-LIN and DoG models give good fits for voxels that are poorly characterized by the P-LIN model (arrows). Voxels for which the cross-validated R^2 of the U-LIN or DoG models was > 5% and at least 5% higher the that of the P-LIN or CSS are indicated by the dashed triangle.

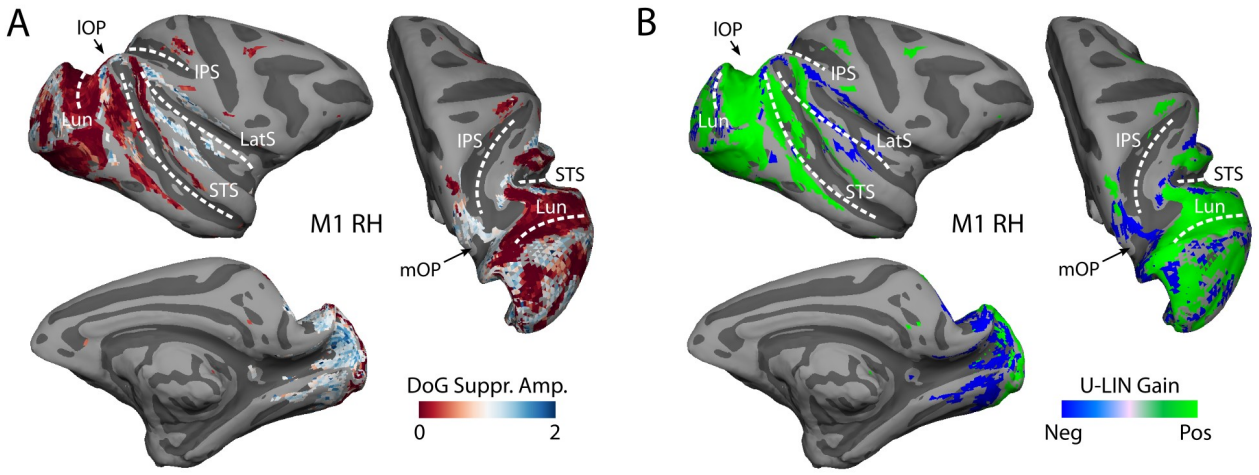

Supplemental Figure 4. (A) Normalized amplitude of the suppressive surround Gaussian of DoG model fits (R^2 > 5%). Values larger than one (blue tints) indicate that the amplitude of suppressive surround was larger than that of the excitatory center. The right hemisphere of M1 is shown as an example. Voxels with a strong suppressive component were in the medial occipital and parietal cortices, and around the lateral sulcus. **(B)** Gain value of the of U-LIN fits for voxels with R^2 > 5%. Green tints represent positive gain values, blue tints indicate suppressive BOLD responses. Negative gain values occur for the same voxels that have a strong suppressive surround in (A) indicating that activity of these voxels is suppressed by visual stimuli.

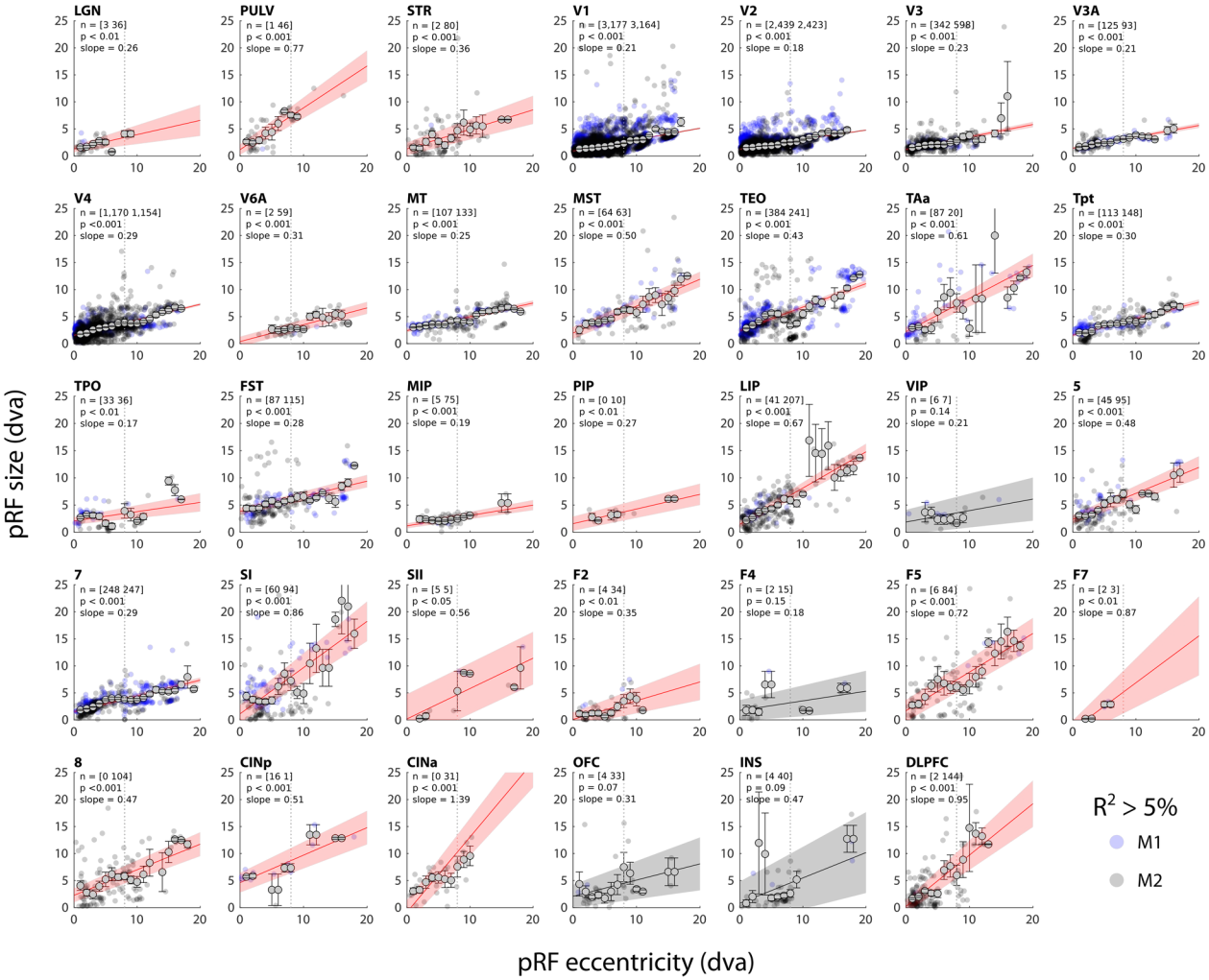

Supplemental Figure 5A. Eccentricity-size relationship for all ROIs. Linear fits (intercept and slope) to the eccentricity-size relationship per brain area. Shaded areas indicate the 95% confidence interval of the fit, *n* denotes the number of voxels (R^2 > 5%). Linear fits in red have a significant slope ($p < 0.05$). Small data-points indicate pRFs for individual voxels (M1 in blue, M2 in black) while larger data-points with error bars indicate binned averages (2 dva bins) over all voxels. The dotted vertical line indicates the extent of the visual stimulus.

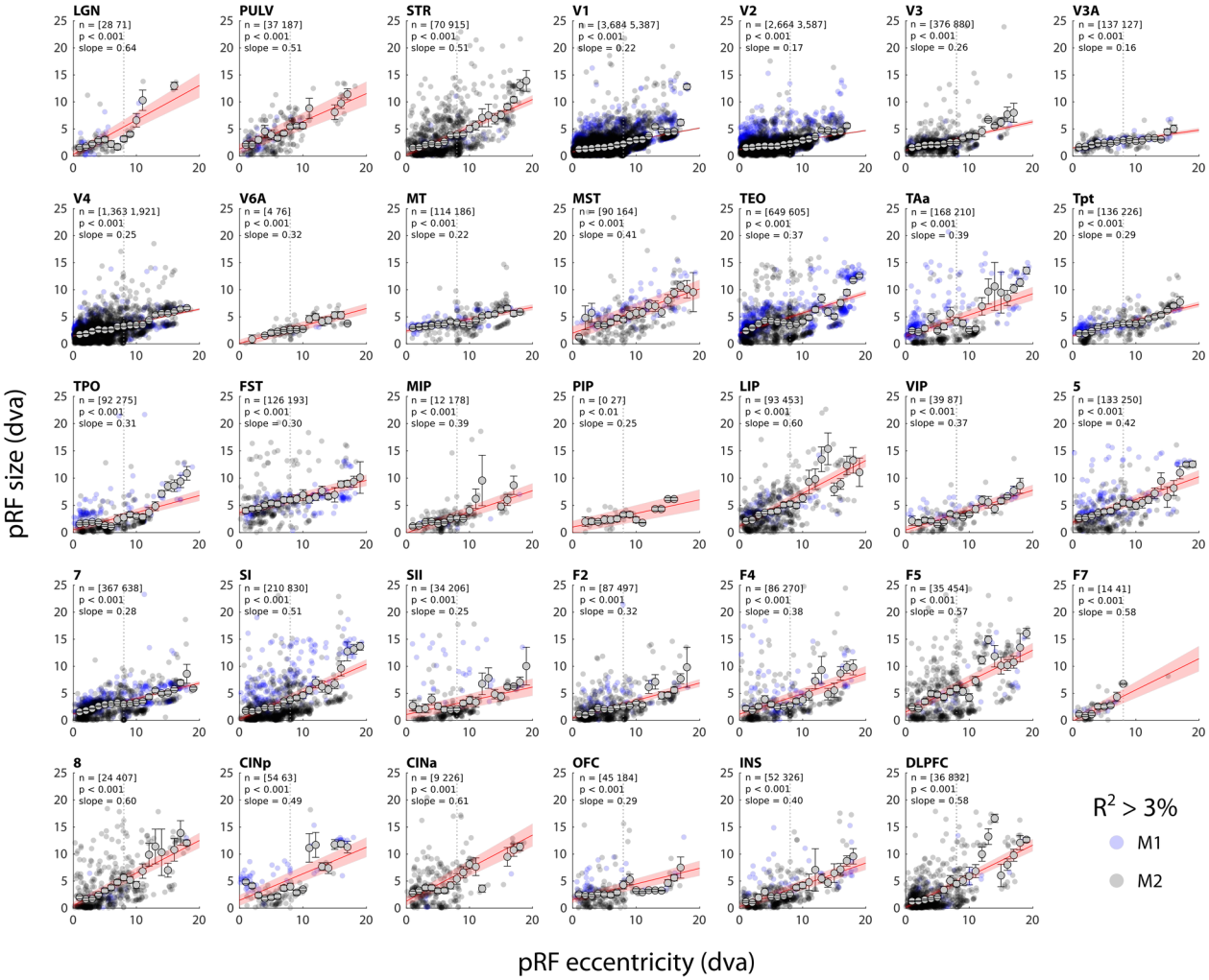

Supplemental Figure 5B. Eccentricity-size relationship for all ROIs. Linear fits (intercept and slope) to the eccentricity-size relationship per brain area. Shaded areas indicate the 95% confidence interval of the fit, *n* denotes the number of voxels (R^2 > 3%). Linear fits in red have a significant slope ($p < 0.05$). Small data-points indicate pRFs for individual voxels (M1 in blue, M2 in black) while larger data-points with error bars indicate binned averages (2 dva bins) over all voxels. The dotted vertical line indicates the extent of the visual stimulus.

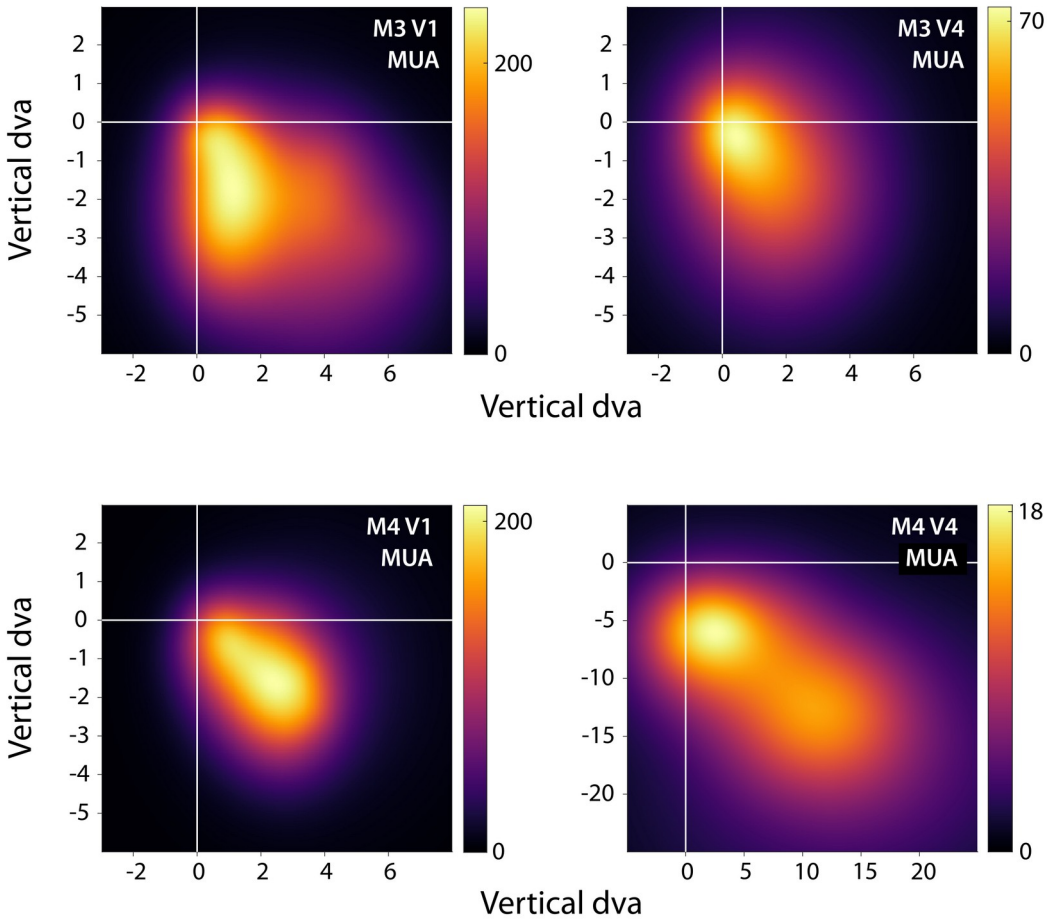

Supplemental Figure 6. Heatmaps of visual field coverage of the Utah arrays. We reconstructed the MUA pRFs with R^2 > 50% in the CSS model in the visual field, normalized them to their peak value, and then summed them across recording sites. The resulting heatmap represents the visual field coverage of V1 and V4 recording sites. The color scale represents the number of pRFs. See Figure 6 for individual pRF locations.

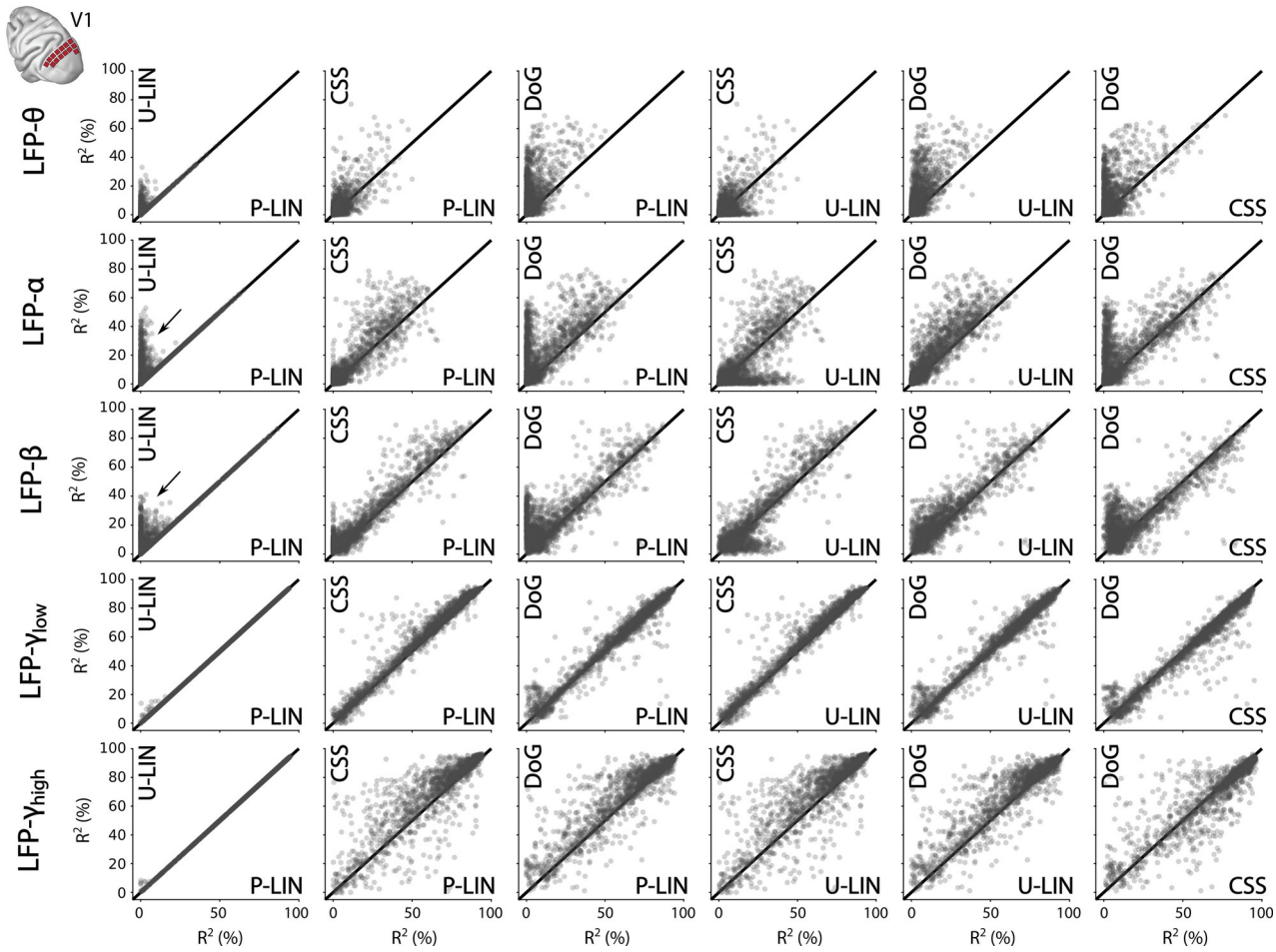

Supplemental Figure 7. Comparison of LFP fits for the four pRF models in V1. Scatter-plots compare R^2 across pRF models and LFP frequency bands. Each dot represents an electrode. For a subset of electrodes, the pRF models that can capture negative responses (DoG, U-LIN) fit better to the lower frequency components of the LFP (α, β) (e.g., arrows in left-most column comparing P-LIN and U-LIN fits).

794

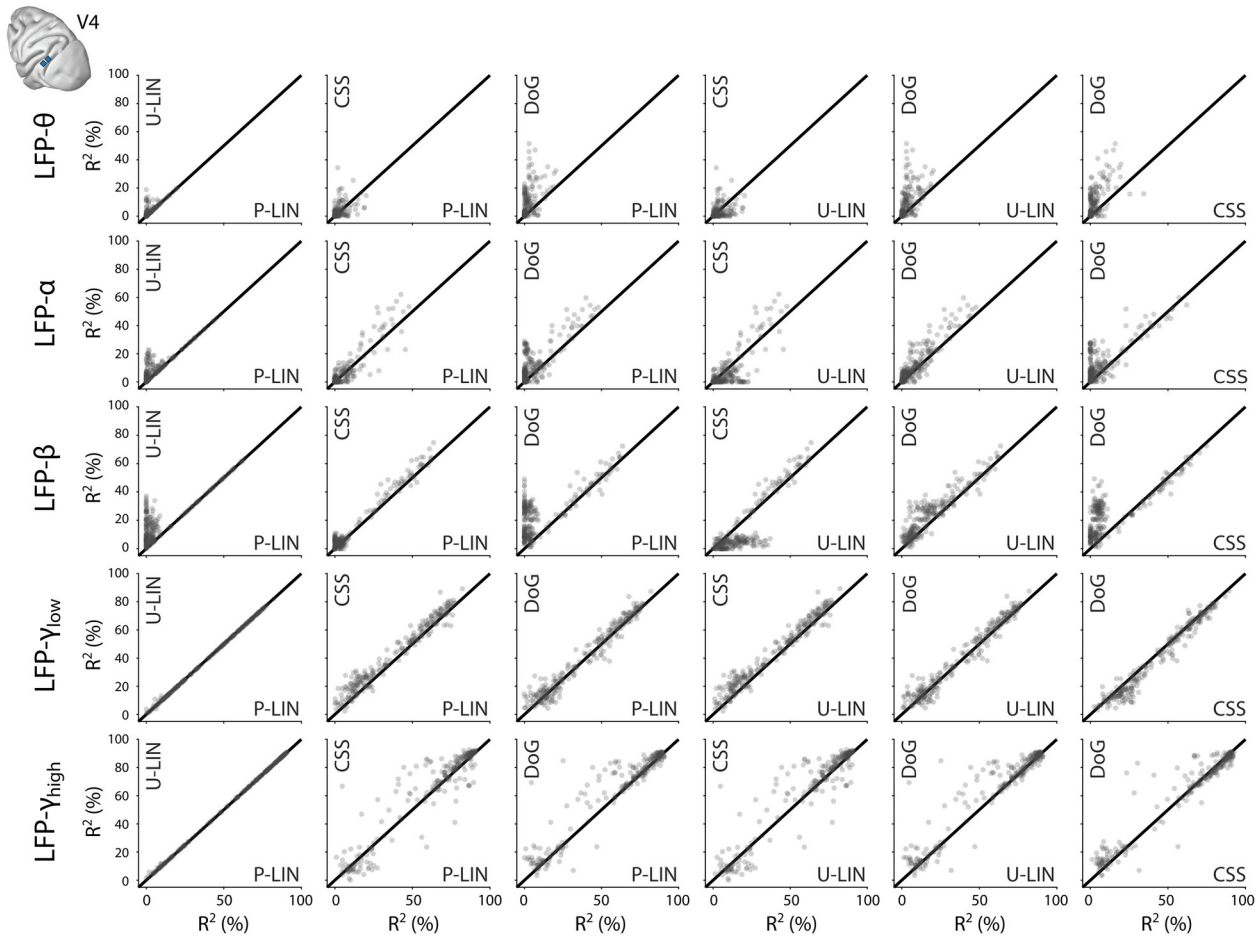

Supplemental Figure 8. Comparison of LFP-based fit results from the four pRF models in V4. Scatter-plots comparing R^2 across pRF models and LFP frequency bands. Each data point represents an electrode.

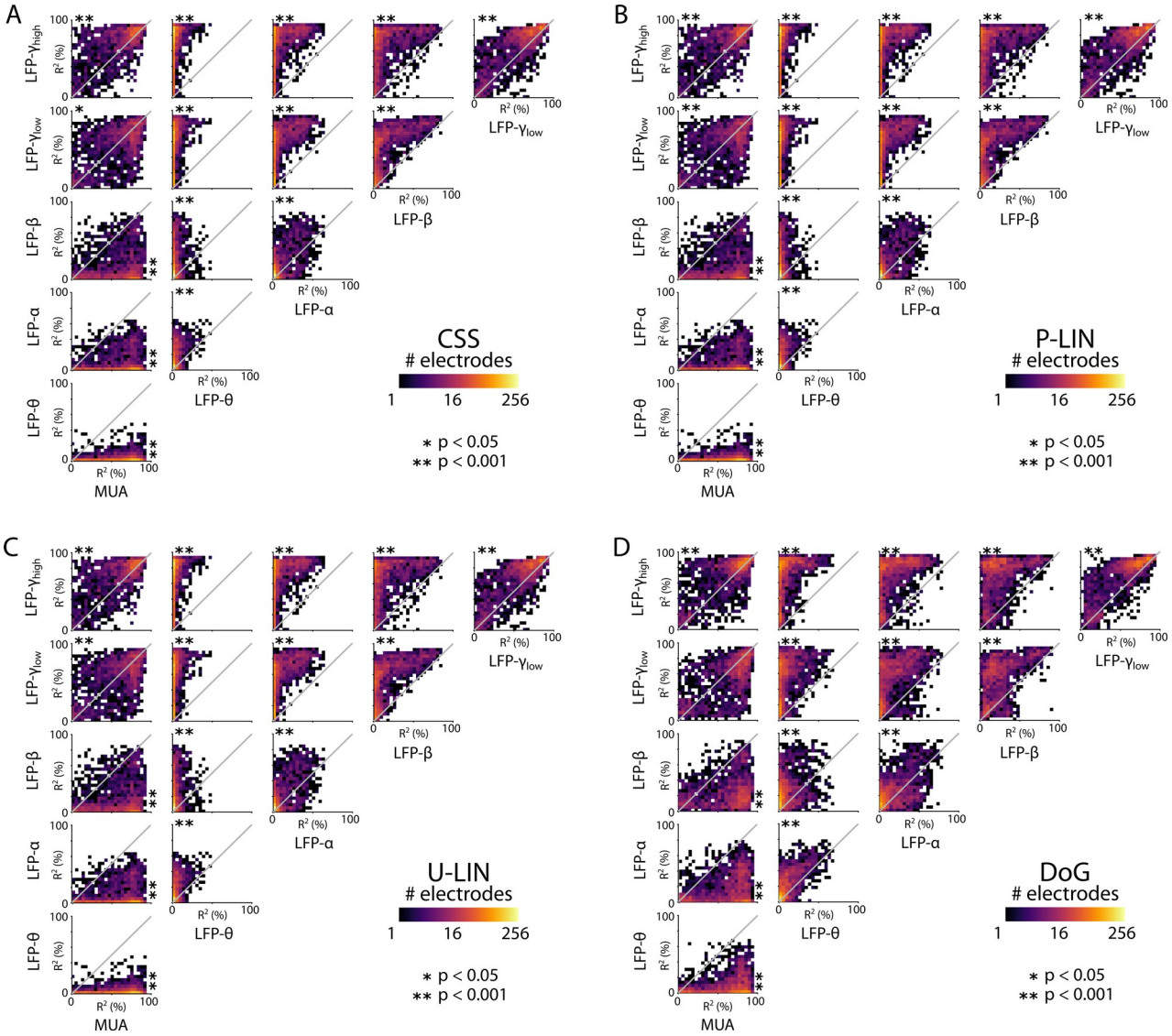

Supplemental Figure 9. Comparison of pRF fit accuracies for MUA and LFP signals at the same recording sites. (A) Comparison of R^2 values from the CSS model across electrophysiological signals. Colors indicate the number of recording sites in 4 × 4 % bins (logarithmic scale). Asterisks denote significance (Kruskal-Wallis, with post-hoc Tukey's HSD multiple comparisons of mean rank, *p < 0.05, **p < 0.001). **(B-D)** Same as in (A) but for the P-LIN (**B**), U-LIN (**C**), and DoG models (**D**).

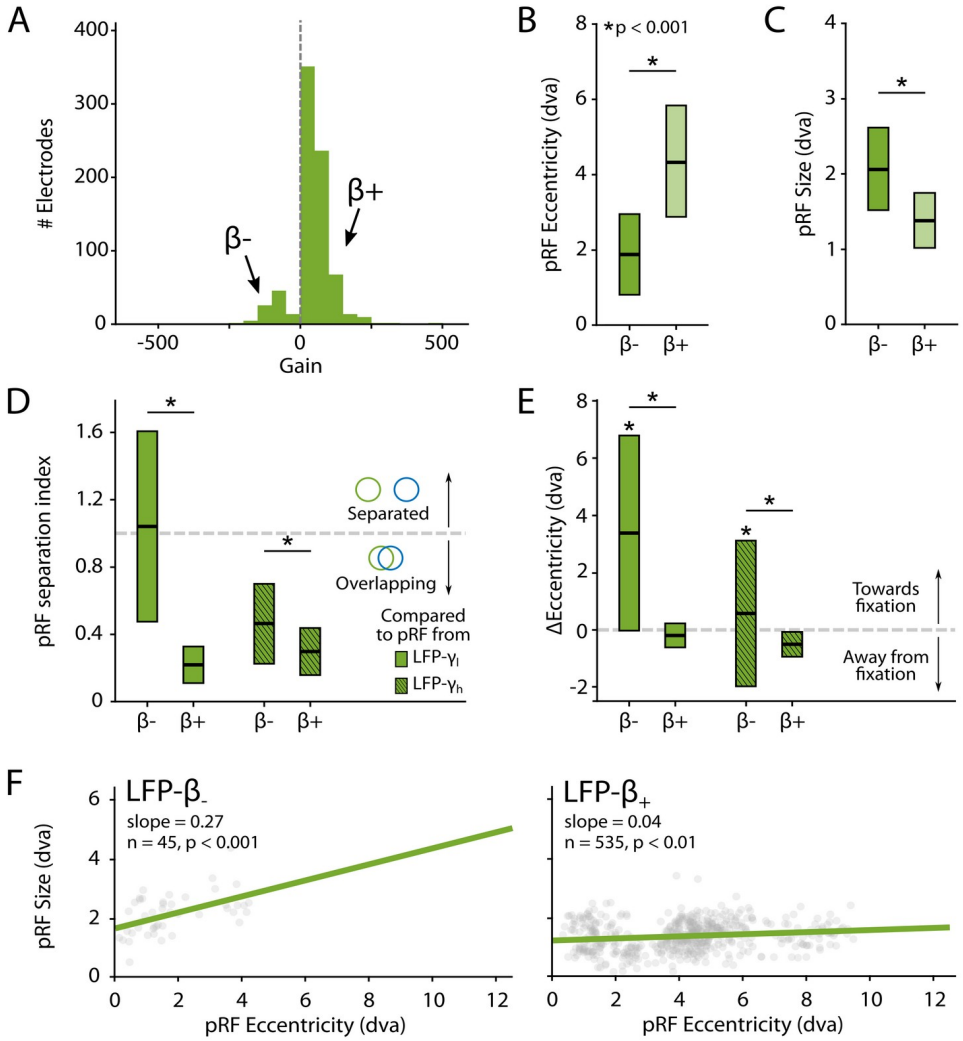

Supplemental Figure 10. Characteristics of LFP-β pRFs in V1 split by positive and negative gain values. (A) Distribution of gain values for LFP-β pRFs of V1 electrodes estimated with the U-LIN model. Recording sites with positive gain pRFs are classified as β+, sites with negative gain pRFs as β-. **(B-C)** PRF eccentricities (**B**) and size (**C**) for β- and β+ electrodes (yellow shades). Colored boxes indicate IQR and the median is shown as a thick horizontal line. Wilcoxon Rank Sum tests were used for comparisons between β- and β+ electrodes. **(D)** Distance between the centers of LFP-β and LFP-γ pRFs from the same electrode, divided by the sum of their respective sizes. Values smaller than one indicate overlapping receptive fields. Non-shaded boxes are comparisons with LFP-γ_{low} pRFs, shaded boxes are comparisons with LFP-γ_{high} pRFs. **(E)** Difference in eccentricity between LFP-γ and LFP- β pRFs from the same sites (calculated as Ecc_{γ}-Ecc_{α}). Positive values indicate that LFP- β pRFs are closer to fixation than LFP-γ pRFs. Wilcoxon Signed Rank, one-tailed test (ΔEcc > 0), for individual cases; Wilcoxon Rank Sum test for comparisons between β- and β+ electrodes. See Supplemental Figure 11 for a visualization of the shifts per recording site. **(F)** Eccentricity-size relationship for β- (left) and β+ (right) electrodes. Dots indicate individual electrodes.

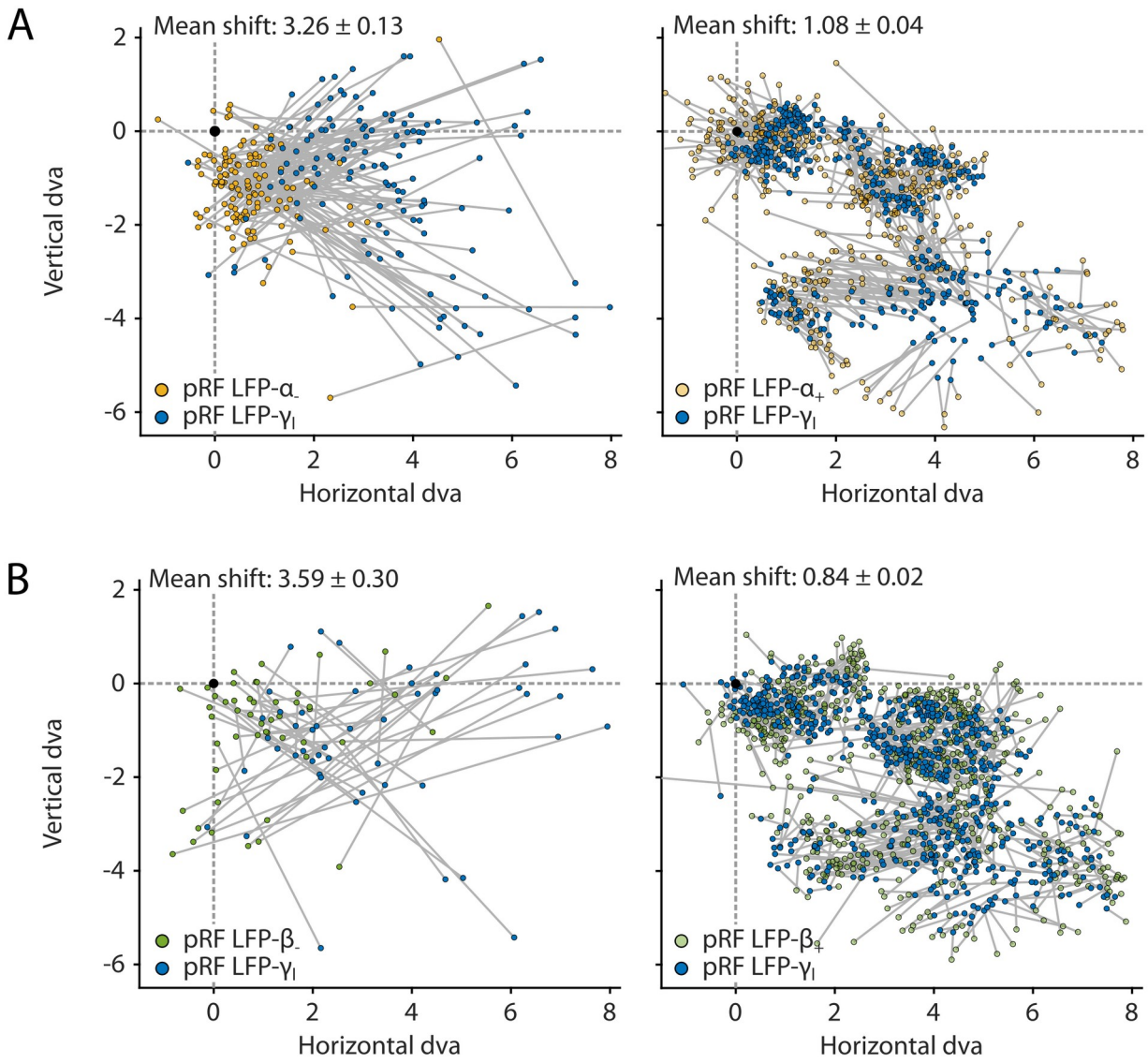

Supplemental Figure 11. Negative pRFs based on low-frequency LFP components are shifted towards the fixation point compared to the positive pRFs based on the high-frequency LFP at the same recording site. (A) Relative locations of pRFs derived from LFP-α (yellow) and LFP-γ_l (blue) of the same recording sites. **(B)** Relative locations of pRFs derived LFP-β (green) and LFP-γ_l (blue) of the same recording sites. Data-points from the same sites are connected with a gray line. The location of the fixation point is indicated with a black dot. The mean shift size ± SEM is listed in each panel. The same data was used to calculate the eccentricity shifts that are summarized in Figure 10E and Supplemental Figure 10E.

801

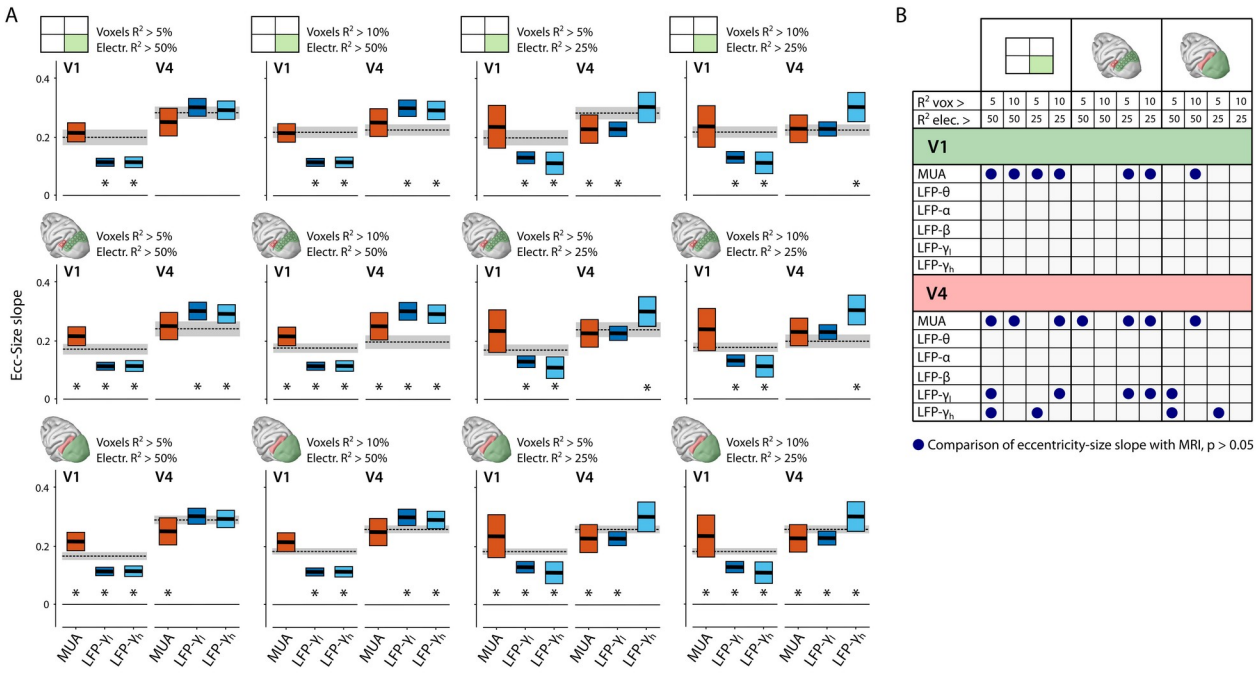

Supplemental Figure 12. Cross-signal comparisons of pRF eccentricity-size relationship. (A) The results of the cross-signal comparisons of CSS-pRF based eccentricity-size slopes for different data inclusion criteria. For the top row, we only included V1 and V4 voxels with pRFs in the lower right visual field where we had electrode coverage. For the middle row we only included voxels corresponding to the location of the electrode arrays. For the bottom row we included all V1 and V4 voxels. Columns indicate different combinations of R^2 threshold level for inclusion of selected voxels and electrodes. The black dashed line and gray area indicate the slope and 95% CI for the MRI-based pRFs; black horizontal lines and colored boxes denote the estimated slope for electrophysiology signals and their 95% CI. Asterisks indicate a significant difference of the eccentricity-size relation between MRI and electrophysiology. **(B)** Summary table of the results in **(A)**, for all electrophysiology signals. Blue dots indicate the inclusion criterion for which the eccentricity-size slope of the pRFs from an electrophysiology signal was not significantly different from that of the MRI signal.

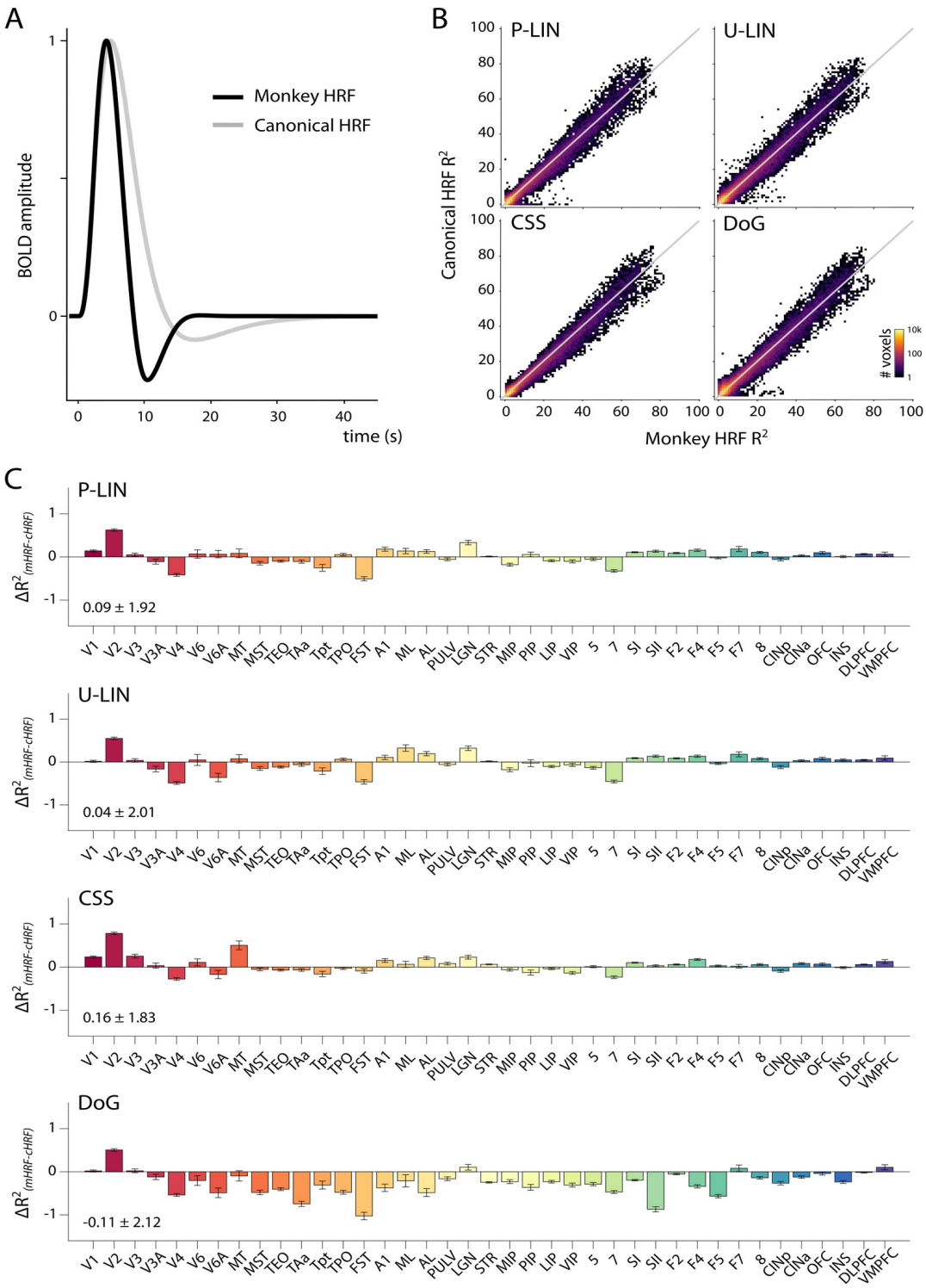

Supplemental Figure 13. Comparison of hemodynamic response functions (HRFs). (A) pRF models were fit to the BOLD response with a monkey-specific (see Materials and Methods) and a canonical HRF provided by the analyzePRF toolbox. The monkey HRF (black line) had a faster decay and more pronounced negative component than the canonical HRF (gray line). **(B)** The choice of HRF had a relatively small effect on the R^2 of the models. The color map in this binned scatter-plot (1 × 1 % bins) indicates the number of voxels. For the P-LIN and CSS models, there was a small but significant advantage of using the specific monkey HRF over a canonical HRF in terms of the percentage of variance explained (Wilcoxon Signed Rank, P-LIN: $z = 8.41$, $p < 0.0001$; CSS: $z = 16.39$, $p < 0.0001$). For the DoG model, the canonical HRF fits were consistently better in all areas except for the early visual areas resulting in a significant advantage across all voxels overall ($z = -29.79$, $p < 0.0001$). For the U-LIN model, the difference between HRFs was not significant for the analysis across all voxels ($z = 0.97$, $p = 0.33$). In all cases however, the effect sizes

were very small ($mean_{(mHRF\text{-}dHRF)}$ ± standard deviation, P-LIN: 0.09 ± 1.92%, U-LIN: 0.04 ± 2.01%, CSS: 0.16 ± 1.83%, DoG: -0.11 ± 2.12%) and the estimated pRF sizes and locations were highly comparable across HRFs ($Size_{(mHRF\text{-}dHRF)}$, P-LIN: -0.07 ± 1.10 dva, U-LIN: -0.05 ± 1.68 dva, CSS: -0.19 ± 7.66 dva, DoG: -0.19 ± 1.68 dva; $Eccentricity_{(mHRF\text{-}dHRF)}$, P-LIN: -0.07 ± 2.13 dva, U-LIN: -0.09 ± 2.30 dva, CSS: -0.02 ± 1.93 dva, DoG: -0.08 ± 2.43 dva). For this reason, we only included the results obtained with the faster monkey-specific HRF in post-fit analyses of the MRI results. **(C)** Mean difference in R^2 value between the HRF's for all models and ROI's. The monkey HRF produced slightly better fits in early visual areas for all models. For the DoG model, the canonical HRF fit slightly better in higher cortical areas. Number in lower left corner the mean R^2 difference (HRF_{monkey} - $HRF_{canonical}$) ± standard deviation.